



ATC-CES

METALLURGICAL REPORT

October 18, 2018

EXAMINATION OF A BOILER CIRCULATION PUMP SHAFT



ATC PROJECT-18B071

PREPARED FOR:



PREPARED BY:

**ATC
COMBUSTION ENGINEERING SOLUTIONS
200 COMPRESS STREET
CHATTANOOGA, TENNESSEE 37405**

October 18, 2018

METALLURGICAL REPORT:

Examination of a Failed Boiler Circulation Pump Shaft



1.0 INTRODUCTION

A fractured shaft, a bushing and a sleeve that had been removed from a boiler circulation pump operating at [REDACTED] were submitted to ATC-CES for metallurgical analysis. [REDACTED] requested that the analysis focus on the shaft due to concerns that deficiencies in the condition of the shaft were responsible for the failure. Figure 1 shows the various pieces of the pump submitted for analysis in the as-received condition. As can be seen, the shaft was submitted in three separate sections, two of which were created by the circumferential fracture and the third by a saw cut which was made to reduce the overall length of the longer of the remaining pieces - see Figure 1. According to background information furnished with the samples, the shaft material was specified to be ASTM A 470, Type 410 supplied in a normalized and tempered condition.

A description of precisely how the sleeve, the bushing and the shaft were assembled in the pump was not provided. However, based on surface markings, including surface coloration, surface scratches and deeper gouge marks, a general understanding of how the various components were assembled within the pump was developed and this understanding has served as the basis for conclusions as to how the failure occurred. The understanding is as follows (reference Figure 1): the sleeve was positioned on the shaft as indicated in Figure 1 and was keyed to the shaft so that the sleeve and shaft rotated together. The bushing was positioned over the sleeve, so that the sleeve rotated within the bushing.

Based on [REDACTED] direction, the metallurgical analysis of the samples had two primary objectives: first, to determine why the shaft had failed, and, second, to determine what type of material, or materials, had been used to fabricate the bushing and the sleeve.

2.0 CONCLUSIONS

The analysis of the shaft established that the shaft had fractured because of a malfunction in the pump that led to severe overheating of the shaft, the sleeve and the bushing. At the fracture location

in the shaft, the microstructure was found to consist of un-tempered martensite across the entire cross-section of the shaft, with the material hardness measuring above 420 HB; this is an indication that the entire cross-section of the shaft had been heated above the upper critical transformation temperature for TP410 steel (~1600°F). In addition, the examination also showed that during the overheating event the grain structure within a surface layer on the shaft approximately ~25 mm deep was visibly coarsened to a size corresponding to ASTM No. 1-2; this is an indication that the temperature at the shaft surface may have reached temperatures as high as 2200°F during the overheating event. Obviously, at such high temperatures the strength of the shaft material would have been substantially reduced, and this weakening almost certainly contributed to the torsional overload of the shaft that was the immediate cause of the failure.

Examination of the fracture surfaces on the shaft showed that the fracture had initiated from the center of the shaft under torsional loading and that 90-95% of the fracture had propagated in an intergranular mode, including the portion of the fracture through the grain coarsened region at the surface of the shaft. This is confirmation of the fact that the fracture occurred during the overheating event and that the intergranular nature of the fracture reflects a ductility-dip response in the material that developed while the shaft material was in the fully austenitic state.

Examination of the shaft at locations away from the sleeve and bushing assembly showed that the microstructure was a “normal” tempered martensite with a hardness in the range of 254–262 HB. At the center of the shaft, the effects of ingotism (i.e., remnants of the original cast structure of the ingot) were observed, including ferrite bands that extended along the entire length of the shaft and solidification shrinkage voids, a few of which were visible on the fracture surface at the center of the shaft. The Charpy V-notch impact test showed that the shaft material (away from the sleeve/bushing assembly) had 15 ft.lbs impact toughness at ambient temperature with >85% intergranular fracture.

In view of the evidence of overheating uncovered in the shaft, a more detailed examination of the sleeve was carried out to better understand the sequence of events that led to the shaft failure. This examination of the sleeve uncovered evidence of significant wear and galling damage on the outer surface where the sleeve was in contact with the inner surface of the bushing. This damage was so severe that the outer surface of the sleeve was partially melted, indicating that surface temperatures exceeded 2700°F. The heat-affected zone produced by the frictional heating extended over more than 85% of the sleeve’s length. In addition to the overheating damage, there was evidence of extensive cracking in the sleeve body that had propagated in both the axial and through-thickness directions.

A limited examination of the bushing also was undertaken to assist in the understanding of the failure events. The bushing material was chemically analyzed and the composition was found to be consistent with a TP420 martensitic stainless steel. Hardness results obtained from the bushing yielded average hardness values in excess of 425 HB, indicating that the bushing also had been heated above the upper critical transformation temperature for TP420 material (>1600°F).

Based on the metallurgical evidence obtained during the destructive examination of the pump components, the following hypothesis has been developed to explain the shaft fracture. It appears

that for reasons unknown at this time, there was a catastrophic interference in movement between the sleeve and the bushing, which resulted in rapid and intense frictional heating of the bushing, the sleeve and the shaft. The heating was so intense that portions of the sleeve material at the contact surface between the sleeve and bushing melted. Metal temperatures in the shaft rose rapidly to levels well above the upper critical transformation temperature for TP410 steel, and under the influence of whatever torsional loads were being applied to the shaft due to its rotation, the shaft fractured in a non-ductile manner due to the limited ductility of the material at the temperatures where the failure occurred (i.e., ductility dip behavior). If this explanation of the events leading to the failure of the shaft is correct, as the available physical evidence suggests is the case, then it can be concluded that the original metallurgical condition of the shaft played no significant role in the shaft fracture.

3.0 SUPPORTING DOCUMENTATION

3.1 Visual Examination

The samples (shaft, bushing and sleeve) were examined visually using a low magnification stereomicroscope in order to identify any features either on the fracture surfaces or on the contacting surfaces between the sleeve and the shaft or the sleeve and the bushing that might be relevant to the failure. With respect to the shaft, as can be seen in Figures 1 and 2, the primary fracture was a circumferential fracture that extended through the thickness of the shaft in the section with the smallest diameter (measured to be approximately 86 mm in diameter); this fracture was non-ductile in character. In addition to the primary circumferential fracture, four axial cracks - also non-ductile - were observed at random locations around the shaft circumference; these axial cracks straddled the circumferential fracture and extended approximately 50-60 mm in the axial direction and as much as 30 mm in the radial direction.

With respect to the contacting surfaces between the sleeve and the shaft and the sleeve and the bushing, the visual examination revealed evidence of severe wear damage and gouging on all contacting surfaces. The conditions of the internal surface of the sleeve and the surface of the shaft where they were in contact are documented in Figures 3 and 4. The pattern of damage observed on these two surfaces was consistent with each other, supporting the conclusion that the damage was a direct result of contact between the surfaces. The conditions of the external surface of the sleeve and the internal surface of the bushing are represented in Figures 5 and 6. As was true with the inner sleeve and shaft surfaces, the pattern of the damage observed on the outer sleeve and inner bushing surfaces was consistent between the two surfaces; this, again, supports the conclusion that the damage observed occurred as the result of contact between those surfaces.

3.2 Fractographic Examination

A more detailed examination of the fracture surfaces was carried out using both a stereoscope and the scanning electron microscope (SEM). The results of the examination are documented in Figures 7 through 14.

As shown in 7 through 9, the primary circumferential fracture was non-ductile in character. The fractographic markings indicated that the fracture had initiated from the center of the shaft and propagated toward the outside surface under the influence of a torsional load. The macroscopic features of the fracture indicated an intergranular-dominated rupture. The axial cracks associated with the failure revealed the same basic fracture features as were observed with the circumferential fracture/cracking.

Examination of the fracture surfaces with the SEM confirmed that the primary fracture was intergranular through the thickness, as illustrated in Figures 10 through 12. It was noted that the average grain size within a surface layer on the shaft (Figure 10) was significantly larger than at locations deeper in the shaft (Figures 11 and 12); this is an indication that the fracture occurred after there had been substantial grain growth as a result of a severe overheating event – (see metallography and Charpy Impact Test for more details). At the center of the shaft, a number of solidification shrinkage voids (casting-type imperfections) were observed, as recorded in Figures 12 and 13.

Separate examination of the axial cracks showed that these cracks also were intergranular in nature, as documented in Figure 14.

3.3 Chemical Analysis

A material specimen was removed from each of the three components (shaft, bushing and sleeve), and these specimens were chemically analyzed to determine the materials involved in the failure. The results of the analyses are presented in Table 1, where it may be seen that the compositions of both the shaft and the sleeve were consistent with the requirements established by ASTM for A 276, Type 410, while the composition of the bushing was consistent with the requirements established by ASTM for A 276, Type 420.

Non-specified and residual elements were at levels where their presence would not have been expected to adversely affect the performance of these components.

3.4 Metallographic Examination

Metallographic specimens were removed from the shaft at the primary fracture site as well as at the opposite end of the shaft so that the macrostructural and microstructural features of the failure and the shaft could be evaluated in detail using light microscopy. In addition, a metallographic specimen was removed from the sleeve in order to better understand the extent of damage in that component. The approximate locations from which the metallographic specimens were removed are indicated in Figures 1 and 5. The results of the metallographic examination are documented in Figures 15 through 26.

The intergranular nature of the primary fracture was confirmed during the examination of these specimens, as shown in Figures 15 through 17. At the fracture site on the shaft, a surface layer that was approximately 25 mm exhibited a coarse-grained structure (ASTM No. 1-2) and fresh martensite (Figure 18). Beneath this grain coarsened layer within the failure area the structure was fine-grained but still consisted of large amounts of fresh martensite, as documented in Figures 19 and 20. In comparison the material at the opposite end of the shaft, well away from the failure area, was uniformly fine-grained with a more “normal” hardness for tempered martensite, as documented in Figures 21 through 23. The metallurgical condition of the shaft material in the fracture area indicates that the entire cross-section of the shaft at the failure location experienced metal temperatures ranging from at least 2200°F in the grain-coarsened surface layer to at least 1600°F beneath the surface layer.

At the center of the shaft, the effects of ingotism were observed with a number of ferrite bands and shrinkage-type voids visible along the entire length of the shaft, as shown in Figures 20 and 23. This type of segregation structure is not uncommon in large diameter steel bar.

The microstructure of the sleeve showed the effects of severe overheating, and it appeared that most of the sleeve had been heated to temperatures above 1600°F, with local areas on the outer surface of the sleeve showing signs of partial melting (temperature >2700°F), as documented as shown in Figures 24 through 26. In addition, the sleeve body contained a substantial number of cracks extending in both the axial and through-thickness directions, with the majority of the cracking being intergranular in nature.

3.5 Hardness Testing

The shaft hardness was measured using both Vickers and Rockwell testing methods. The Vickers testing was conducted on the metallographic specimens with a 500-gram test load, while the Rockwell testing was conducted on a 12 mm thick cross-section of the shaft taken from a location approximately 36 mm away from the fracture and near one edge of the sleeve (therefore, not subject to the most severe overheating conditions). The Vickers test results are documented in Table 2 and the Rockwell test results are recorded in Figure 27.

As shown in Table 2, the hardness values in the vicinity of the shaft fracture all were over 420 HB across the full radius of the shaft; these values are consistent with untempered martensite in TP410 stainless steel and confirm the fact that the material was heated above the upper critical transformation temperature. In contrast, the hardness values at the opposite end of the shaft – well away from the failure area - were in the range of 250-265 HB, which is consistent with a “normal” tempered martensitic structure for this material.

The hardness profile across the radius of the shaft was determined using a Rockwell Hardness Tester in the C-scale range. The test results are shown in Figure 27. As can be seen, the surface layer had hardness values in excess of 380HB while the hardness at the center of the shaft was as low as 195HB. This hardness profile reflects damage at the outer edges of the overheated region where a large temperature variation existed between the surface (>1600°F) and the center (1400°F)

of the shaft. At the shaft surface, the material was heated well above 1600°F to form untempered martensite while at the shaft center the maximum temperature achieved was in the range of 1400°F, resulting in an over-tempered martensitic structure.

3.6 Charpy Impact Testing

Four full-size Charpy V-notch specimens were removed from the shaft, two of which (F1 and F2) were taken near the fracture within the overheated zone and the other two (O1 and O2) were taken from the opposite end of the shaft with no effect of overheating. All specimens were removed at 0.5 radius location and in the L-R direction. All impact tests were conducted at ambient temperature (67°F) and the test results are recorded in Table 3.

As shown, the original shaft (O1 and O2) had Charpy impact toughness 151f.lbs at ambient temperature while the overheated shaft material (F1 and F2) revealed approximately 20 ft.lbs. Fractographic examination of the tested Charpy specimens showed that the fracture of all four specimens was predominantly intergranular, as documented in Figures 28 through 31. These results suggest that in the as-received condition the shaft material was in a moderately temper-embrittled condition. However, based on the overwhelming evidence of catastrophic overheating of the shaft during operation, it is clear that the original metallurgical condition of the shaft played no meaningful role in the shaft fracture.

If you have any questions pertaining to the information presented in this report, or if I can be of any further assistance in this matter, please feel free to call me at 423-267-0647.

Author 
Gang (Joe) Zhou

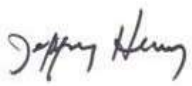
Reviewer 
Jeff Henry

Table 1. Chemistry Results

Chemical Composition (Weight Percent)					
ELEMENT	Shaft	Sleeve	ASTM A 276 Type 410	Bushing	ASTM A 276 Type 420
CARBON	0.15	0.15	0.15 max	0.17	0.15 min
MANGANESE	0.44	0.77	1.00 max	0.78	1.00 max
PHOSPHORUS	0.022	0.019	0.040 max	0.018	0.040 max
SULFUR	0.001	0.001	0.030 max	0.001	0.030 max
SILICON	0.22	0.78	1.00 max	0.79	1.00 max
NICKEL	0.30	0.12	---	0.18	---
CHROMIUM	12.01	12.40	11.5 – 13.5	12.65	12.0 – 14.0
MOLYBDENUM	0.15	0.029	---	0.030	---
VANADIUM	0.069	0.040	---	0.031	---
COLUMBIUM	ND	ND	---	ND	---
TITANIUM	0.001	0.002	---	0.002	---
COBALT	0.023	0.015	---	0.017	---
COPPER	0.073	0.093	---	0.16	---
ALUMINUM	0.003	0.002	---	0.002	---
BORON	0.0010	0.0011	---	0.0012	---
TUNGSTEN	<0.001	<0.001	---	<0.001	---
TIN	0.004	0.004	---	0.007	---
NITROGEN	ND	ND	---	ND	---

Note: ND – Not Determined

Product analysis tolerance over the maximum limit for carbon and nitrogen is 0.002%

Table 2. Hardness Measurements

VICKERS HARDNESS VALUES-HV (HB)* Vickers hardness tester with a 1-kg test load					
<i>Sample</i>	<i>Location</i>		<i>Average</i>	<i>Range</i>	
				<i>Min.</i>	<i>Max.</i>
Micro A	Adjacent to Fracture	Surface of Shaft	454 (427)	440	468
		0.5 Radius of Shaft	450 (425)	449	452
		Center of Shaft	447 (421)	429	461
Micro B	Opposite End of Shaft	Surface of Shaft	276 (262)	270	280
		0.5 Radius of Shaft	277 (262)	274	281
		Center of Shaft	268 (254)	266	271

* The HB numbers are approximate values converted from Vickers Hardness readings using the conversion tables in the ASM Metals Handbook, Desk Edition - 1985.

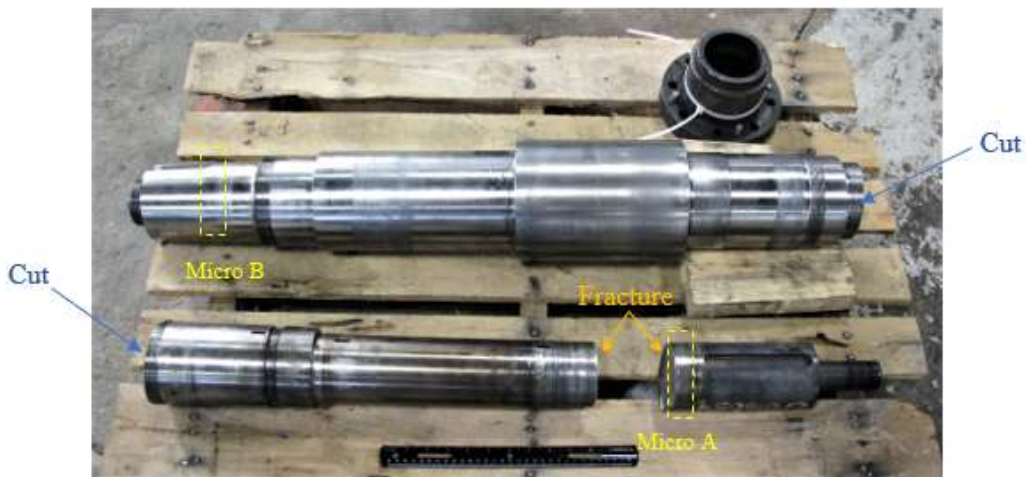


Table 3. Charpy V-Notch Impact Test Results

Charpy V-Notch Impact Test Results <i>with Full-size Specimens</i>				
Sample	Boiler Circulaiton Bump Shaft			
<i>Specimen ID</i>	F1	F3	O1	O3
<i>Specimen Locations</i>	Near Fracture		Opposite End	
<i>Specimen Orientation</i>	Longitudinal (L)			
<i>Notch Orientation</i>	Radial (R)			
<i>Test Temperature (°F)</i>	Ambient (67)			
<i>Energy Absorbed (ft.lbs)</i>	19.5	20.0	15.5	16.0
<i>Lateral Expansion (mils)</i>	15	15	10	10
<i>Percent Shear (%)</i>	7	7	0	0

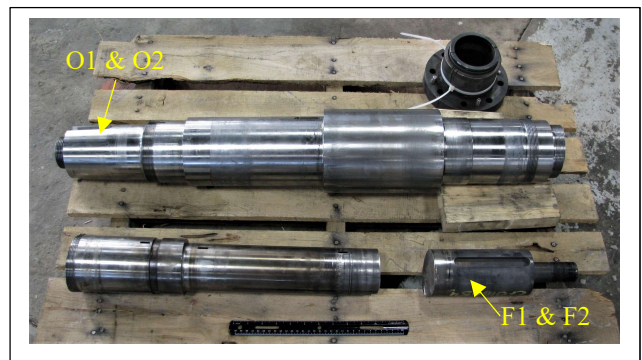
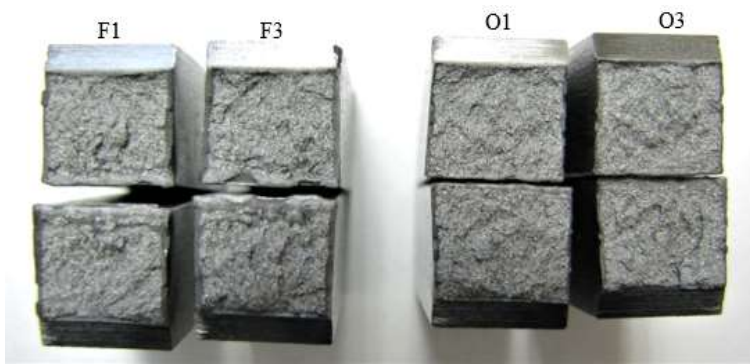




Figure 1. In these photographs, the various pieces of the boiler circulation pump involved in the failure are shown as they appeared when received by ATC-CES. The location of the circumferential fracture in the shaft and the estimated position of the sleeve and bushing on the shaft are indicated. Note the discoloration of the shaft surface at the failed end of the shaft.

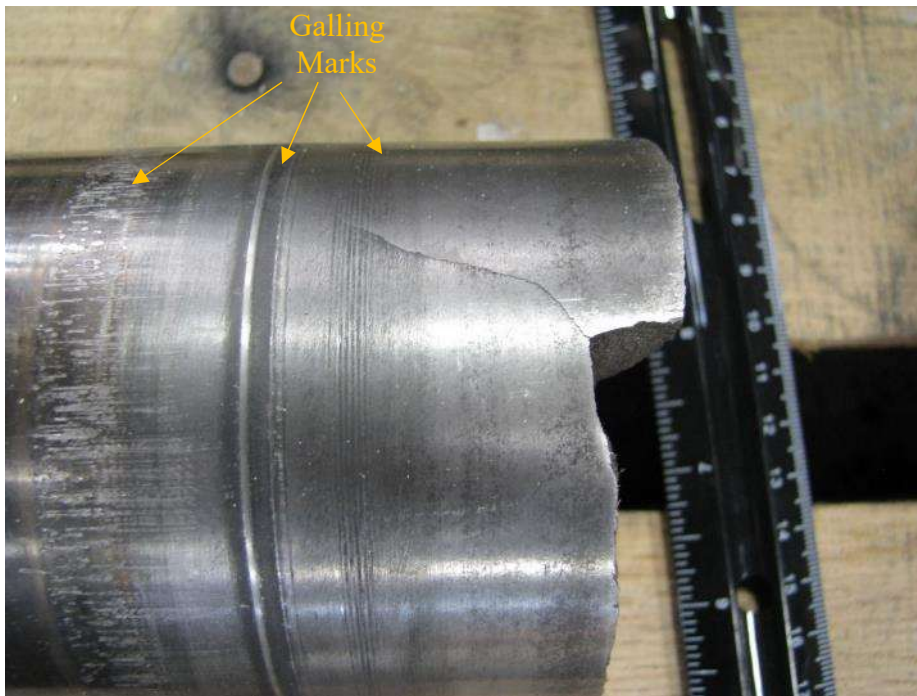


Figure 2. Documenting the general features of the primary fracture that had occurred in the boiler circulation pump shaft.

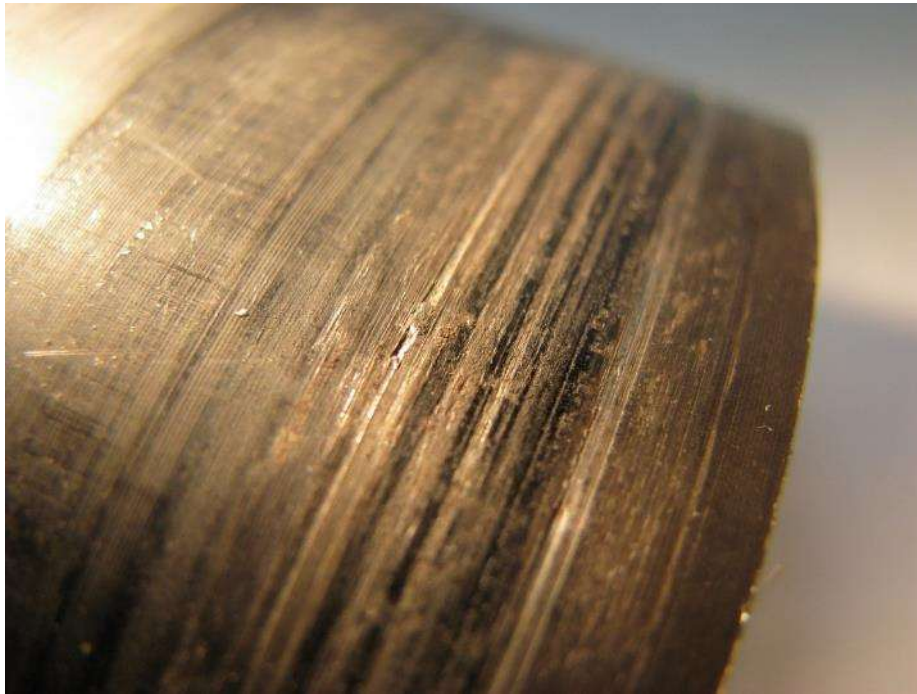
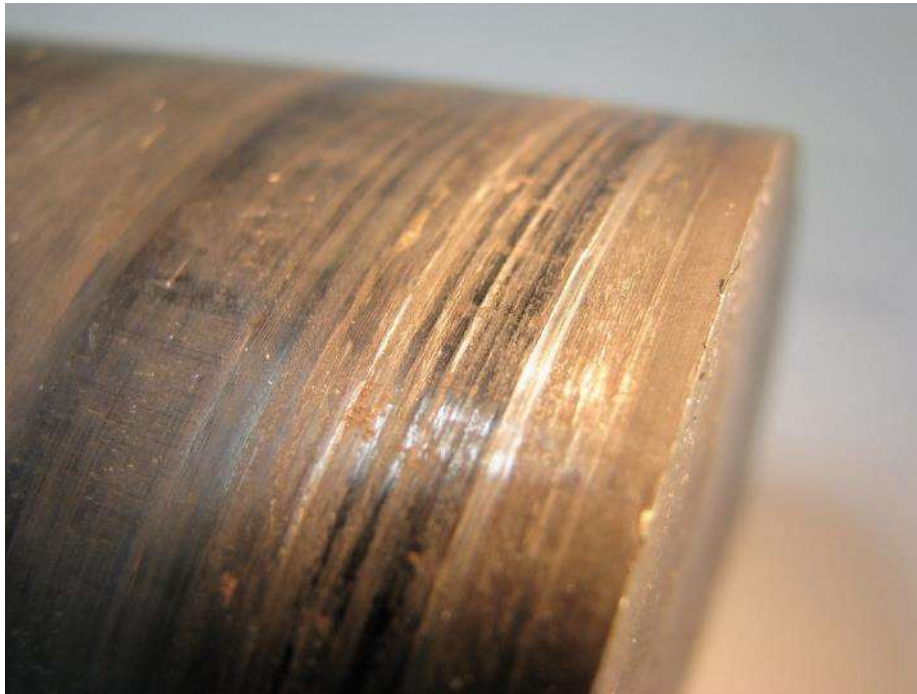


Figure 3. Showing the surface scoring visible on the shaft surface near the fracture.

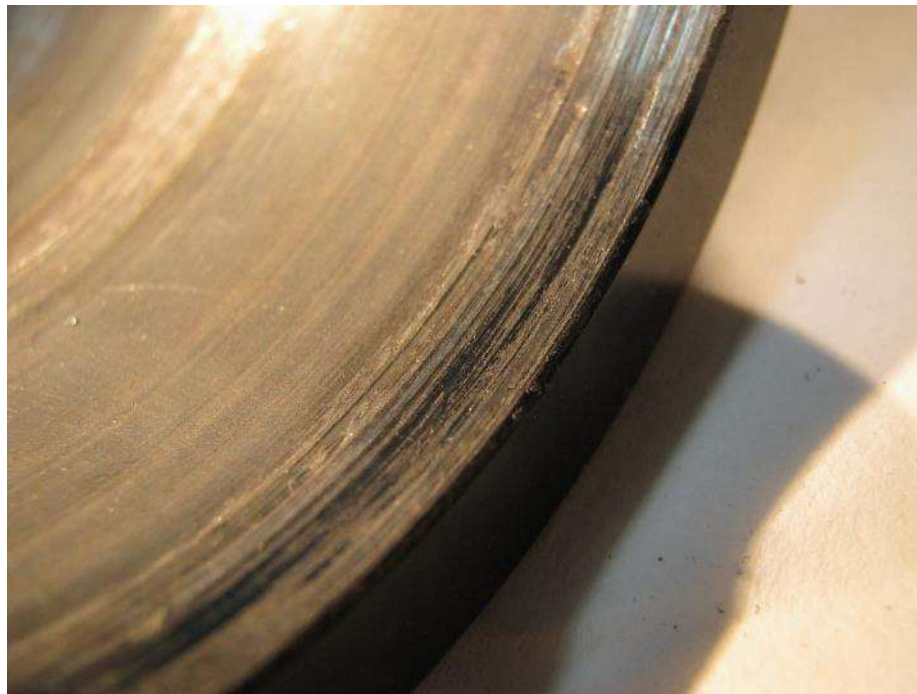
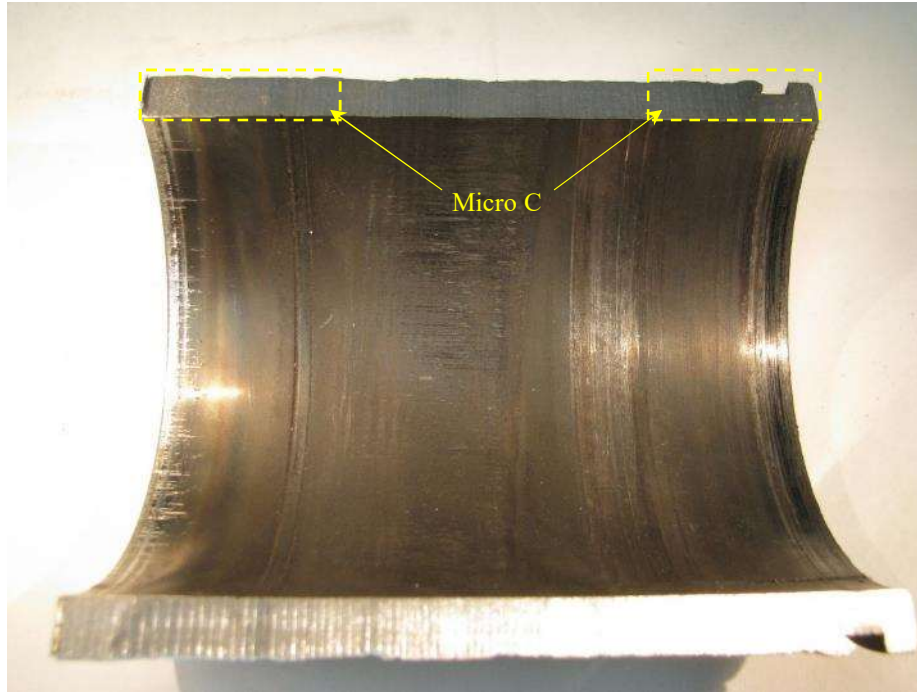


Figure 4. Showing the surface scoring and gall marks visible on the internal surface of the sleeve where it was in contact with the shaft surface.



Figure 5. Showing score marks and deep gouges that were visible on the internal surface of the bushing where it was in contact with the outer surface of the sleeve.



Figure 4. Documenting score marks and deep gouges visible on the external surface of the sleeve where it was in contact with the internal surface of the bushing.



Figure 5. Documenting the general appearance of the primary circumferential fracture in the shaft and showing one of the secondary axial cracks that straddled the primary fracture. Both the axial and circumferential fractures were non-ductile in character.

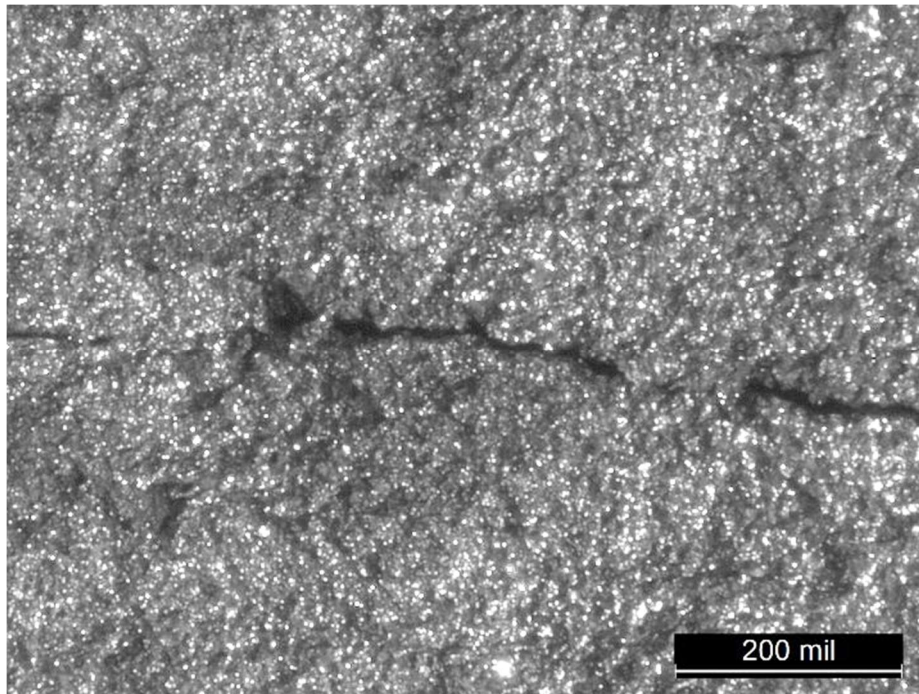
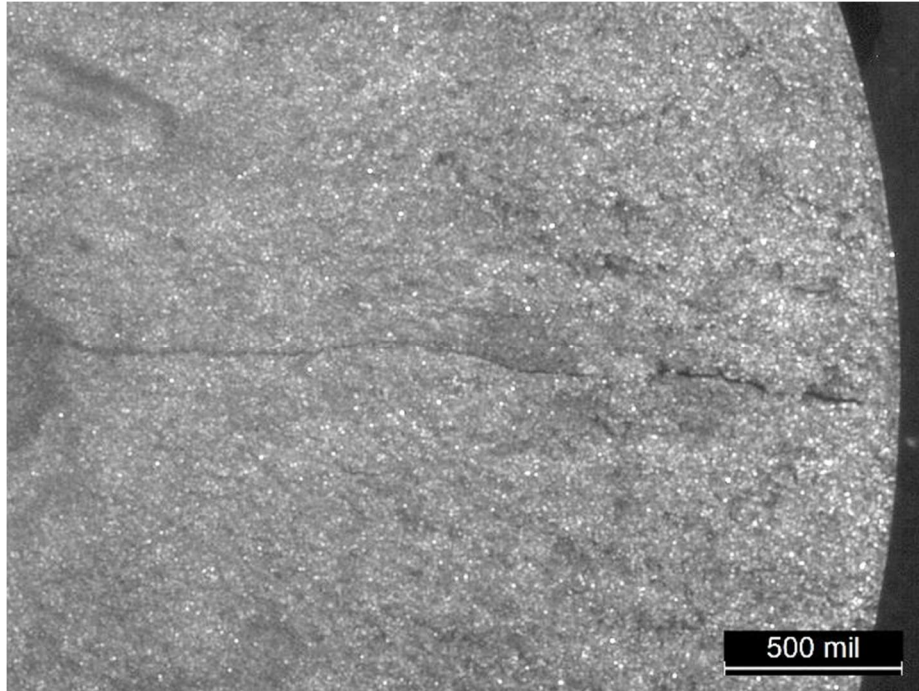


Figure 6. The features of the primary fracture at the edge of the pump shaft are shown here at higher magnifications; the fracture appearance was consistent with an intergranular-dominated fracture.

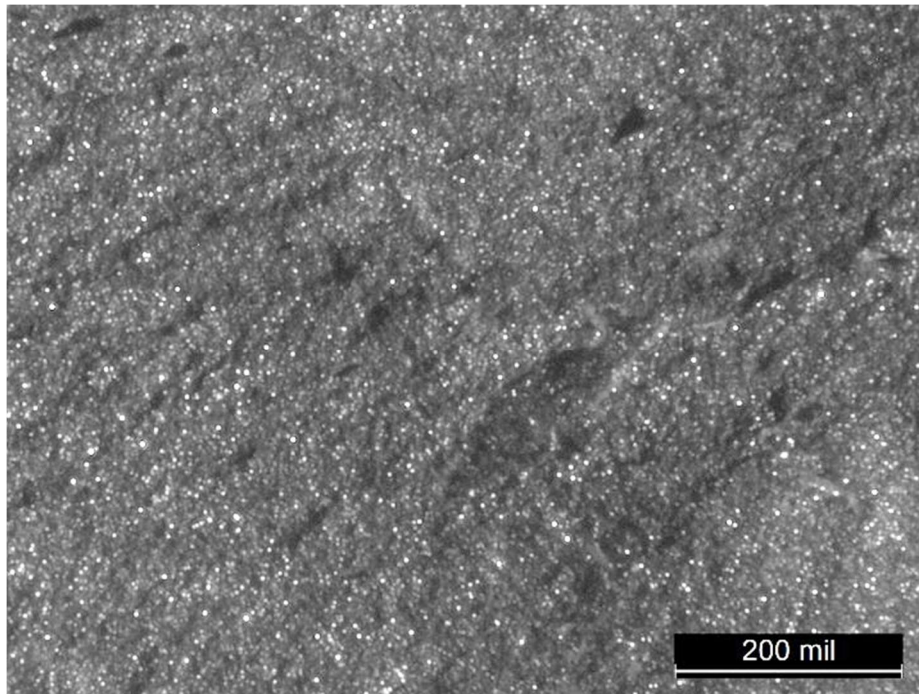
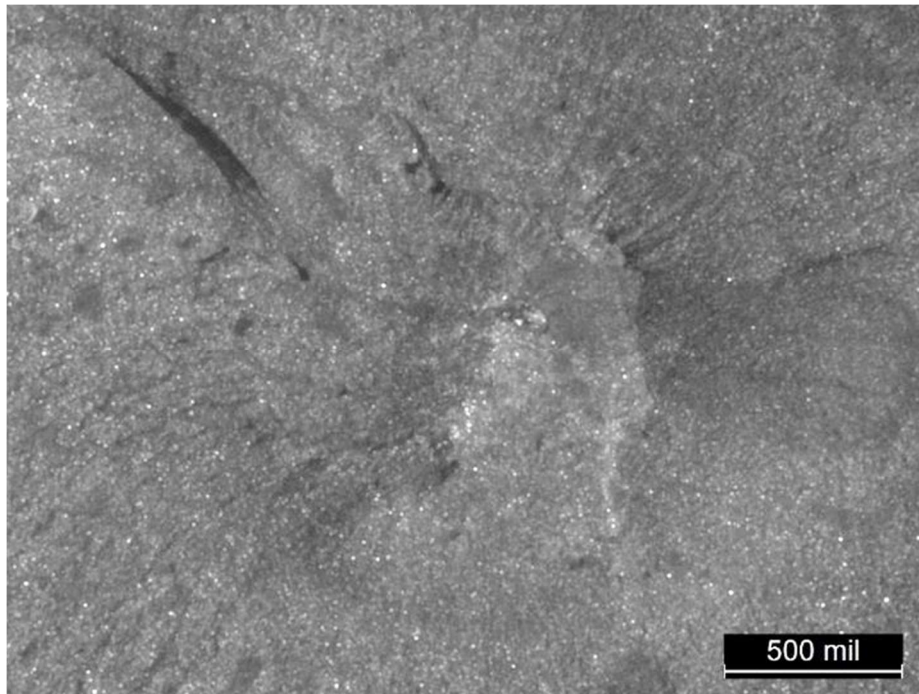


Figure 7. The features of the primary fracture at the center of the shaft are shown here at higher magnifications; the fracture appeared to be predominantly intergranular at this location, as well.

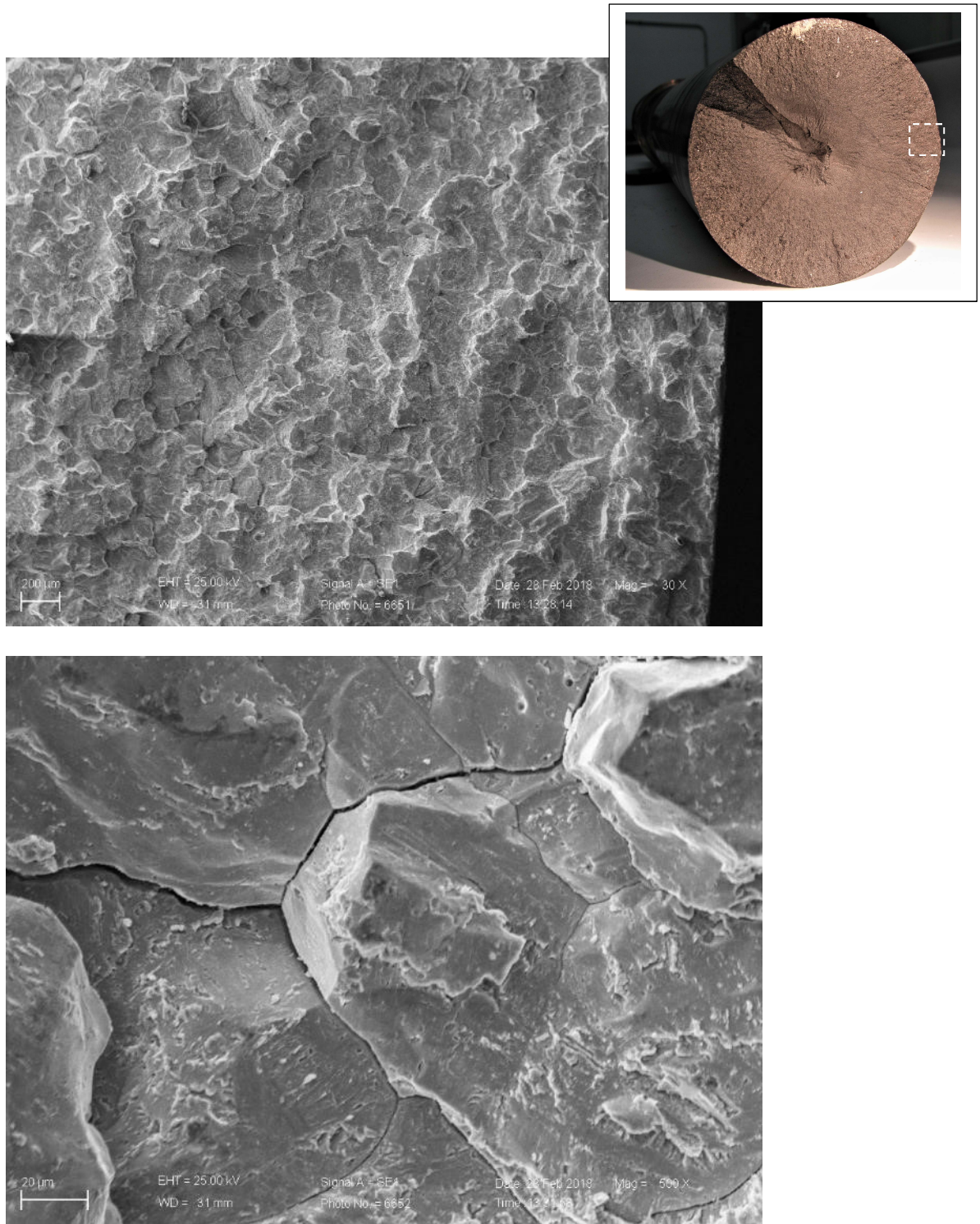


Figure 8. SEM micrographs confirming the intergranular nature of the fracture at the edge of the pump shaft.

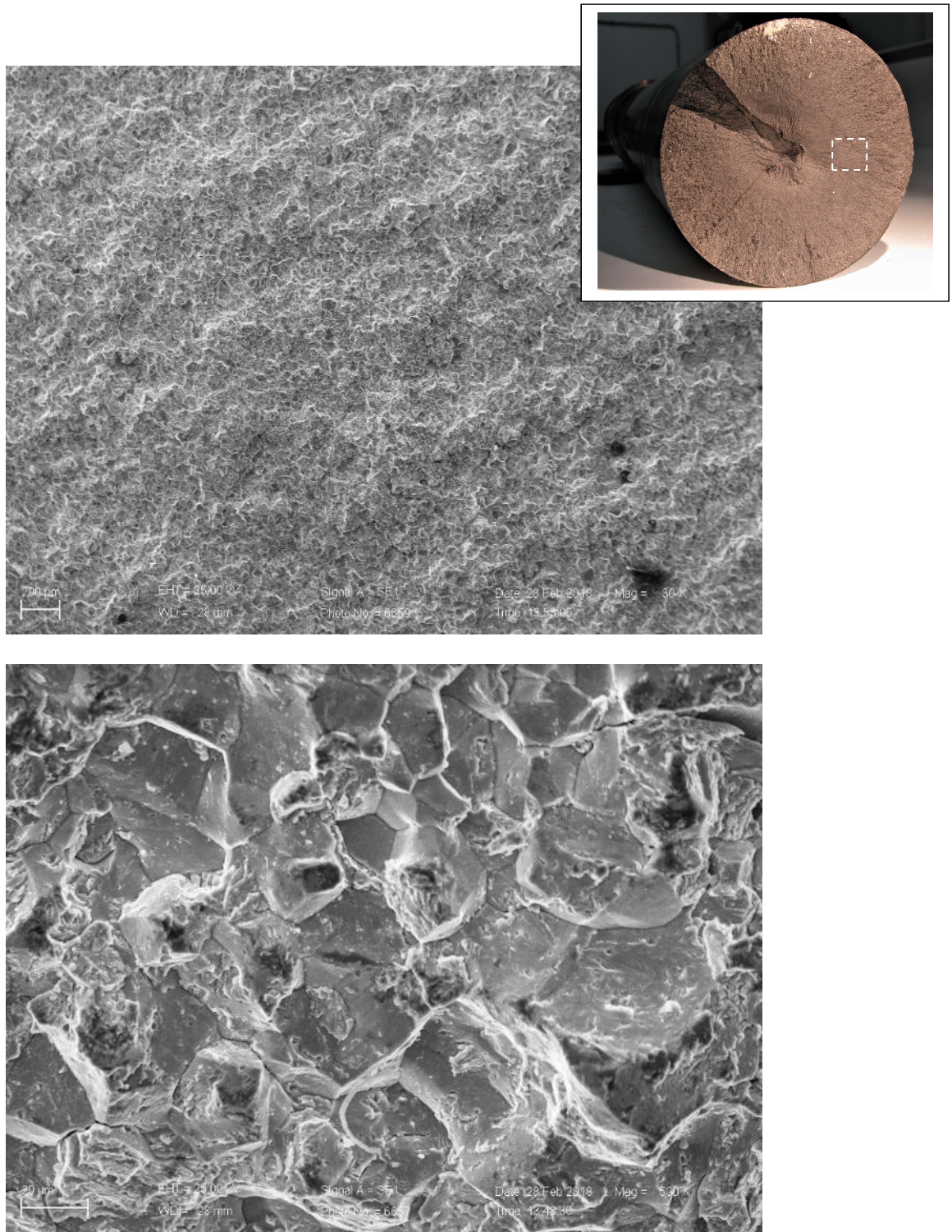


Figure 9. SEM micrographs confirming the intergranular nature of the fracture at the 0.5 radius location of the shaft.

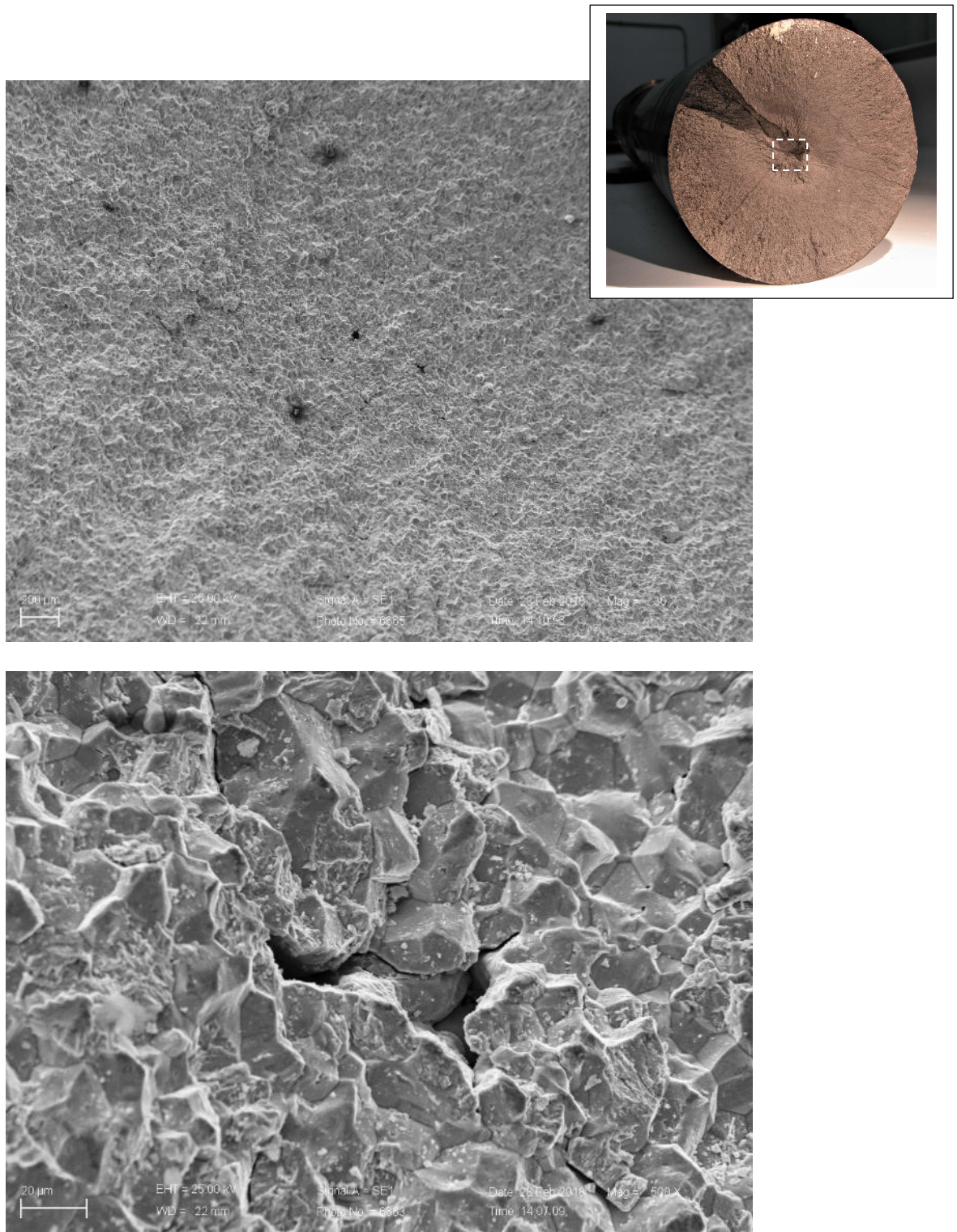


Figure 10. SEM micrographs confirming the intergranular nature of the fracture at the center of the shaft.

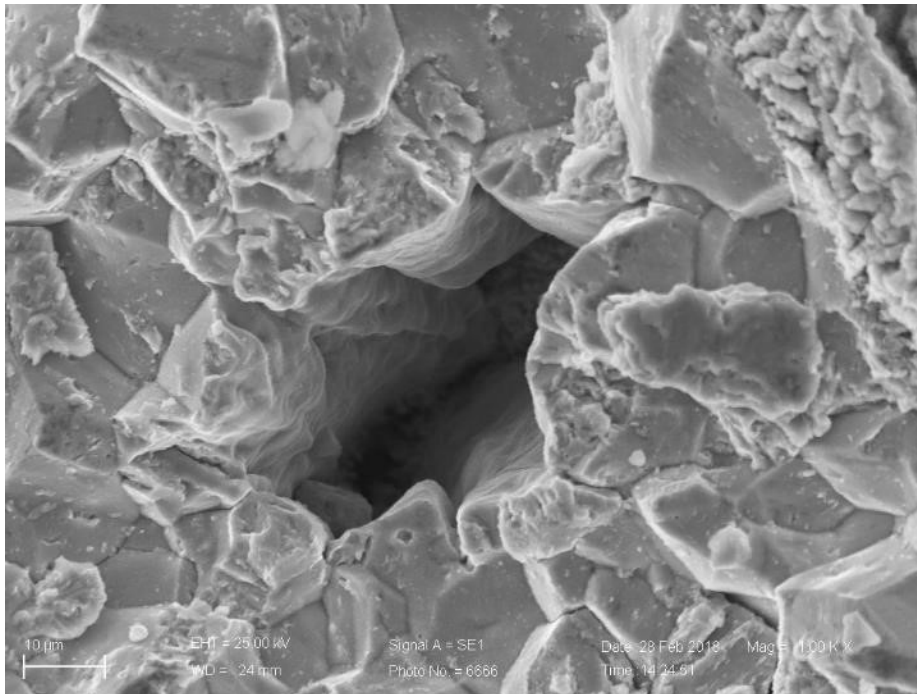
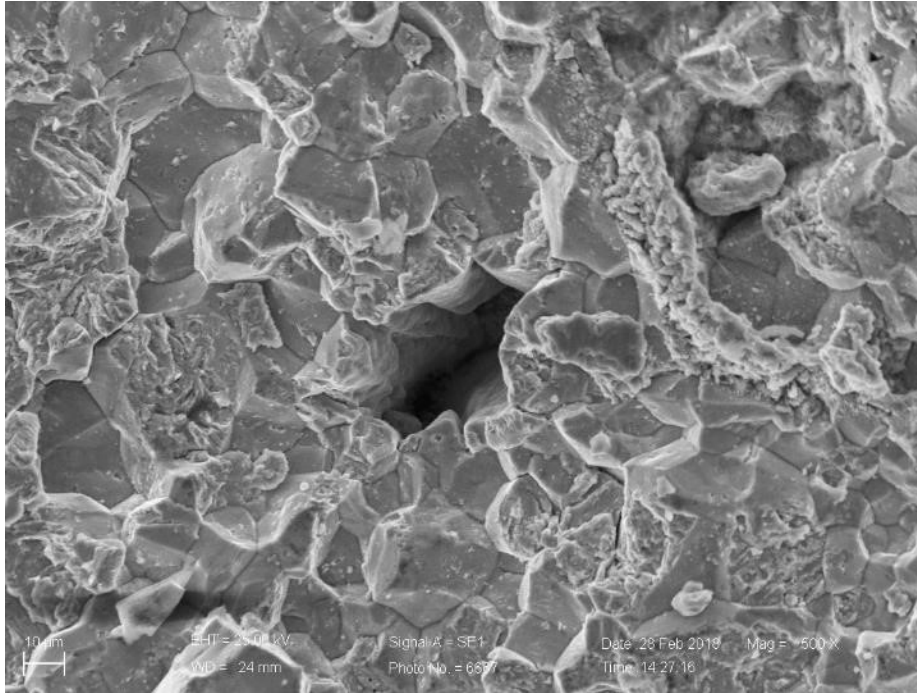


Figure 11. Illustrating solidification shrinkage voids detected in the center area of the shaft, a remnant of casting-type defects that were present in the ingot from which the shaft was produced.

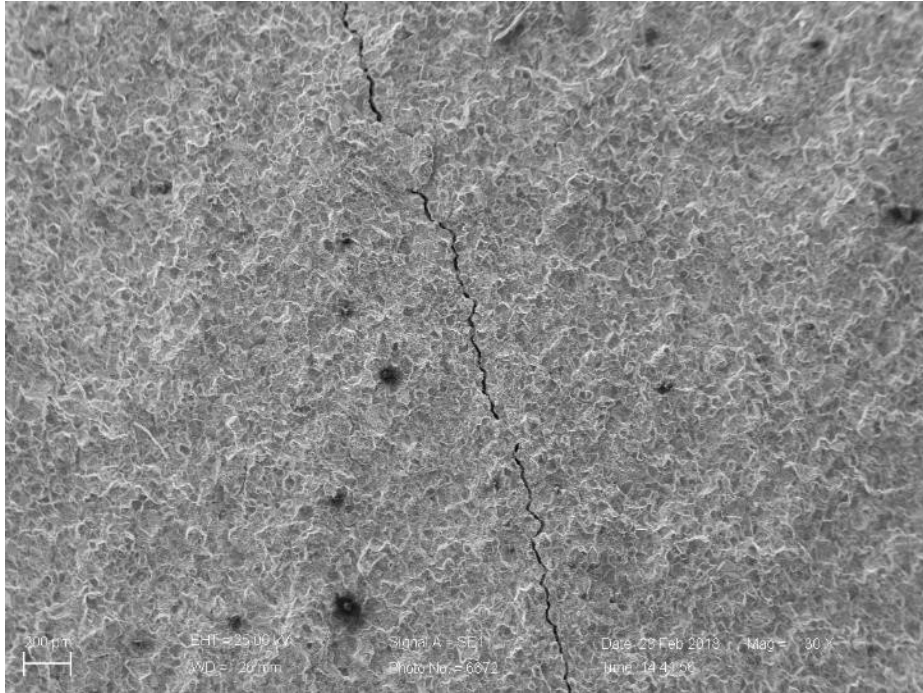


Figure 12. SEM micrographs presenting “typical” features of one of the axial cracks that had formed in the shaft during the failure event.

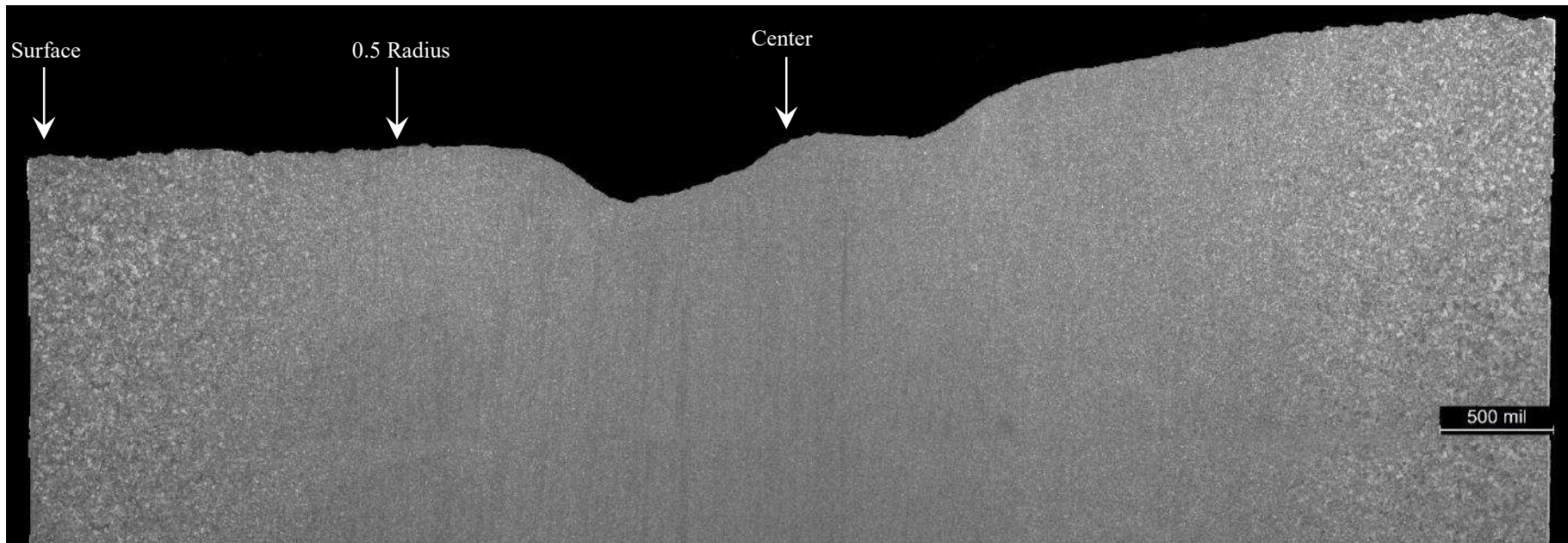
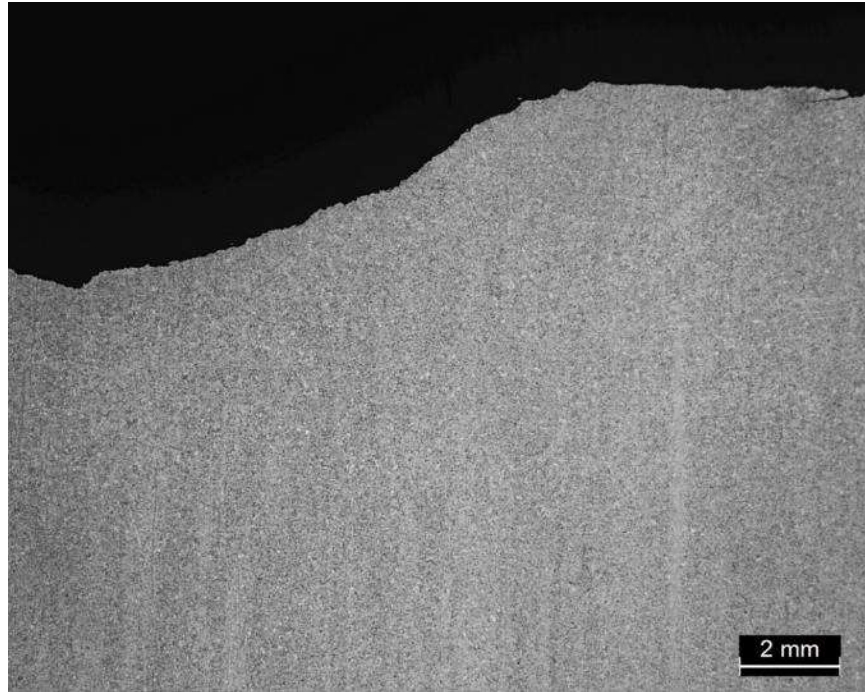
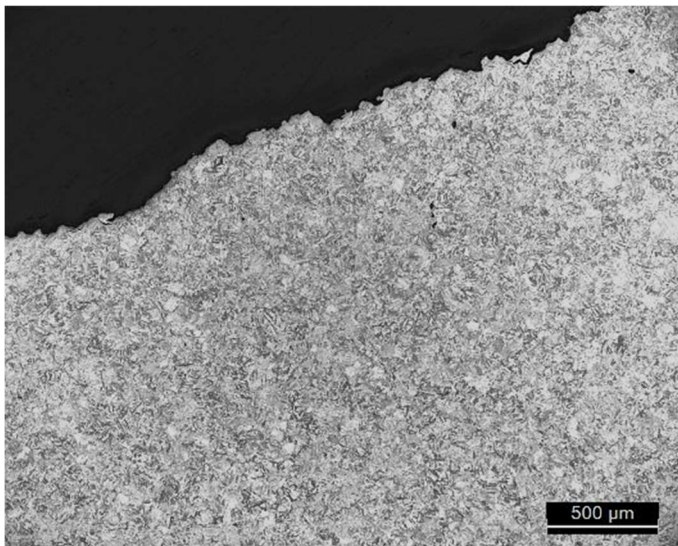


Figure 13. Shown are the macroscopic features of the entire cross-section of the shaft, with the evidence of ingotism in the center portion and coarse-grained structure near the outside surface.

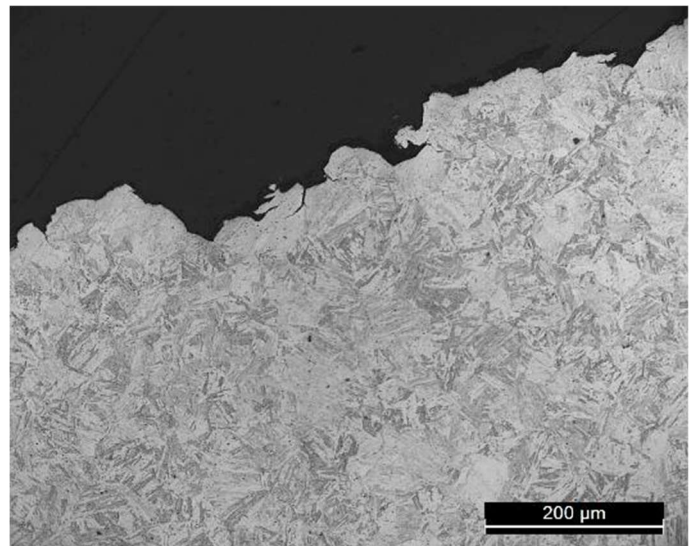


Micro-A
Nital Etch

*Center Portion of
Shaft*

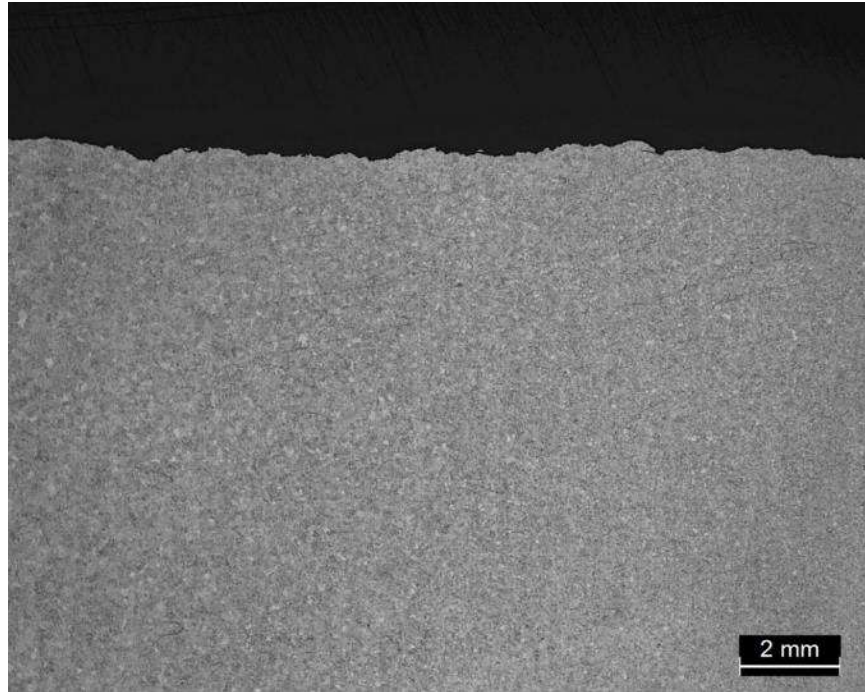


Micro-A



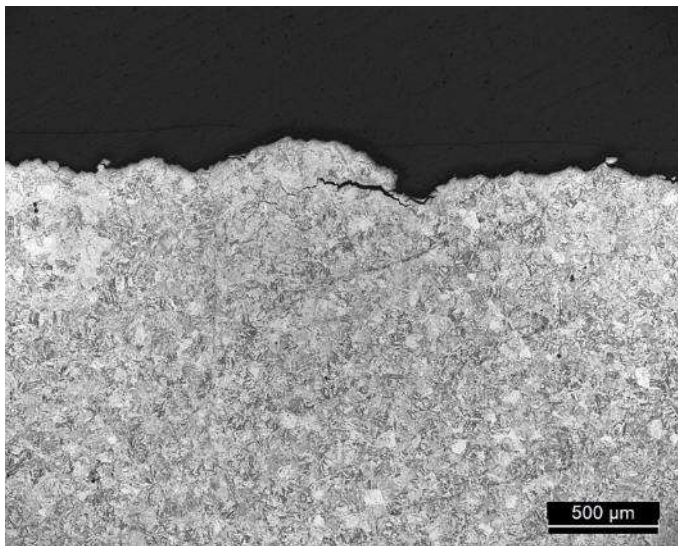
Nital Etch

Figure 14. Documenting typical features of the fracture at the center of the shaft, consistent with intergranular-dominated fracture.

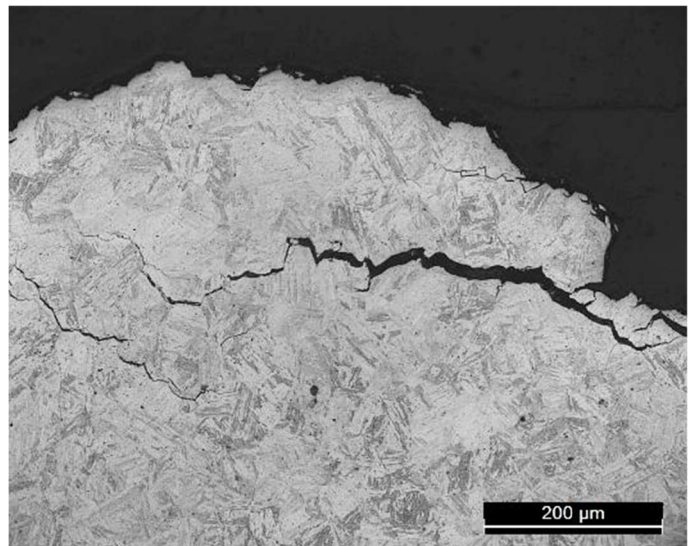


Micro-A
Nital Etch

*0.5 Radius of
Shaft*

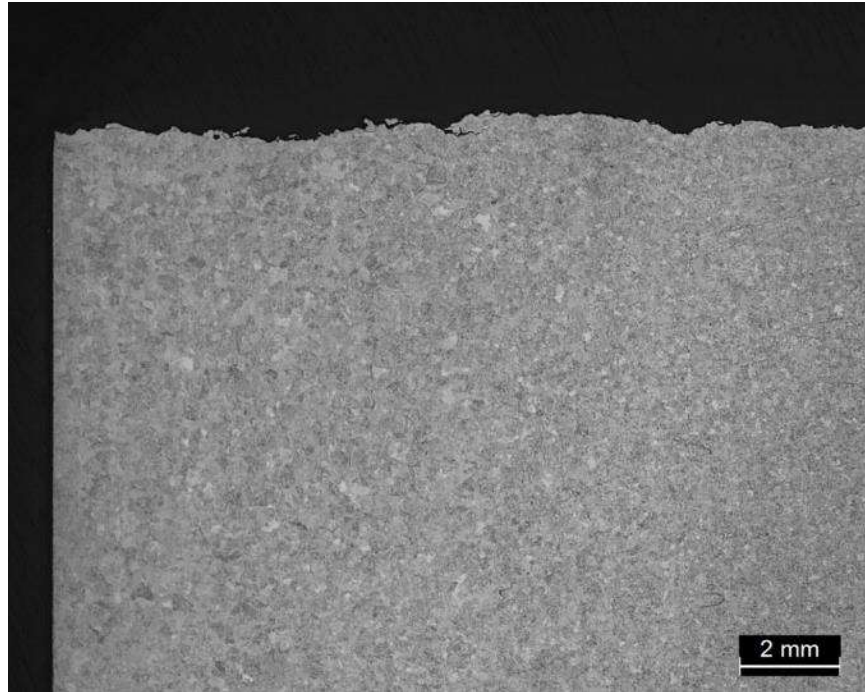


Micro-A



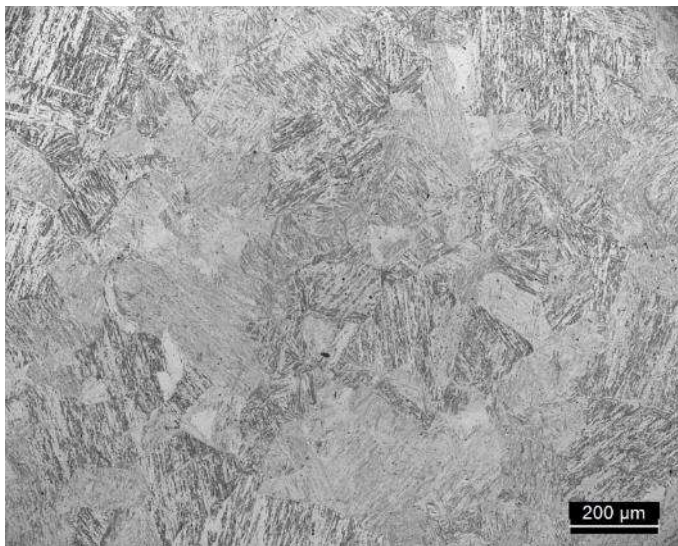
Nital Etch

Figure 15. Showing typical features of the fracture at the 0.5 radius location on the shaft, with evidence of intergranular-dominated fracture.

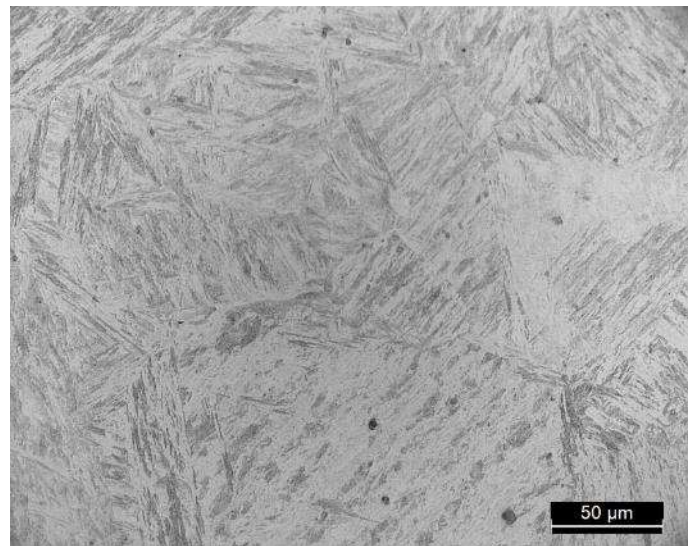


Micro-A
Nital Etch

*Surface of Shaft
at fracture*

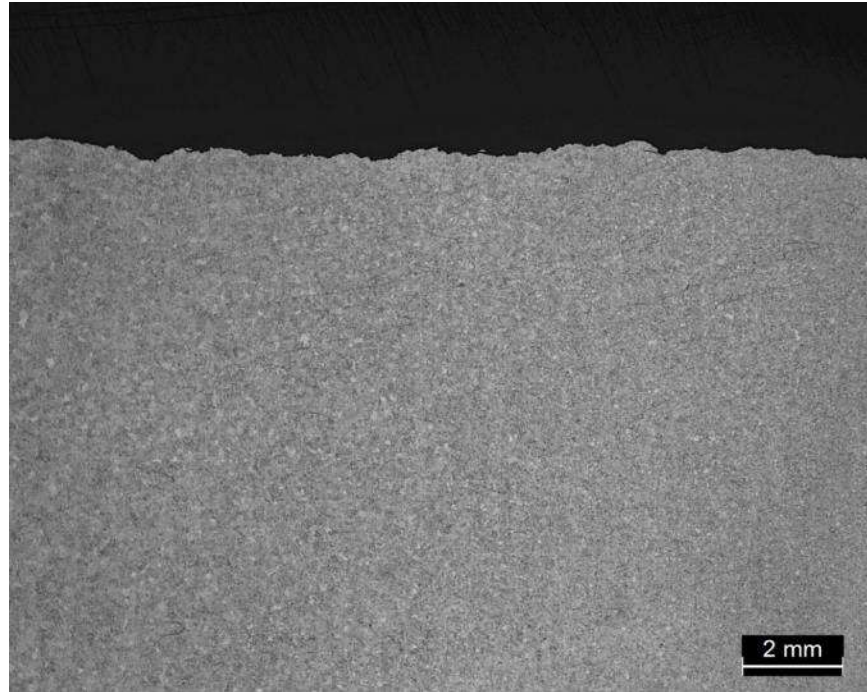


Micro-A



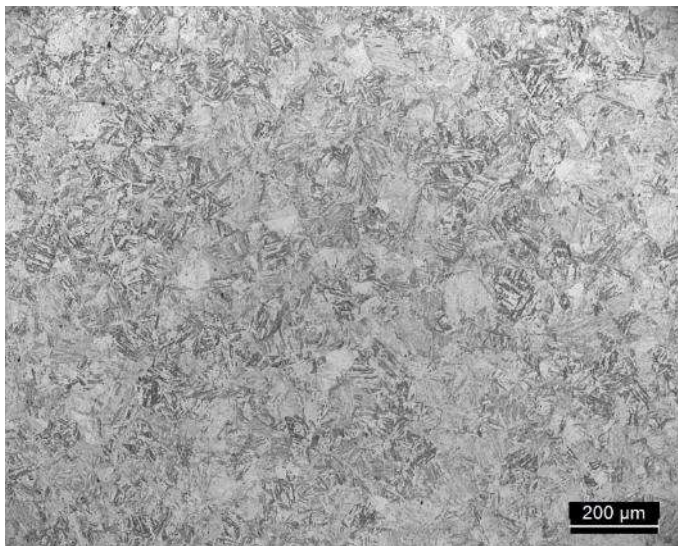
Nital Etch

Figure 16. Showing typical features of the shaft microstructure near the outer surface of the shaft in an overheated layer containing a severely coarsened grain structure.

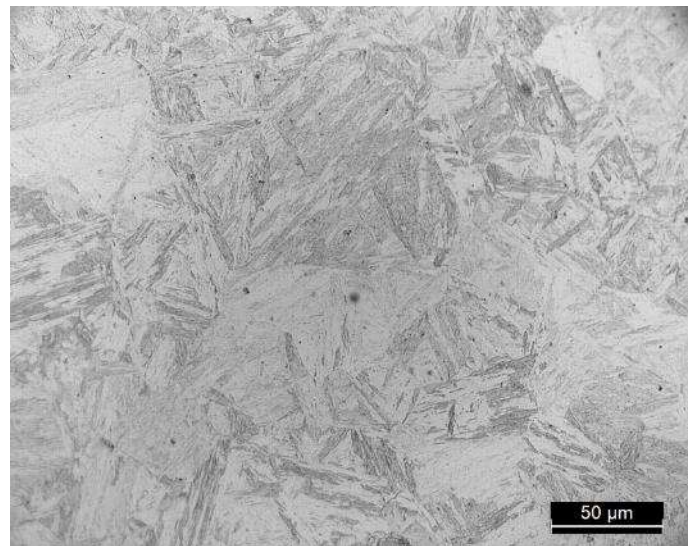


Micro-A
Nital Etch

*0.5 Radius of
Shaft at fracture*

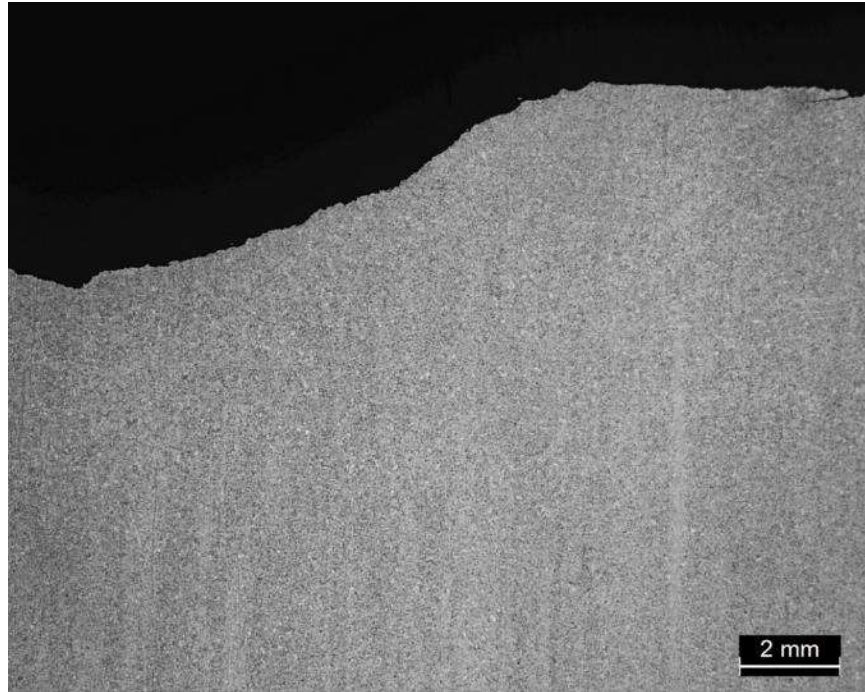


Micro-A



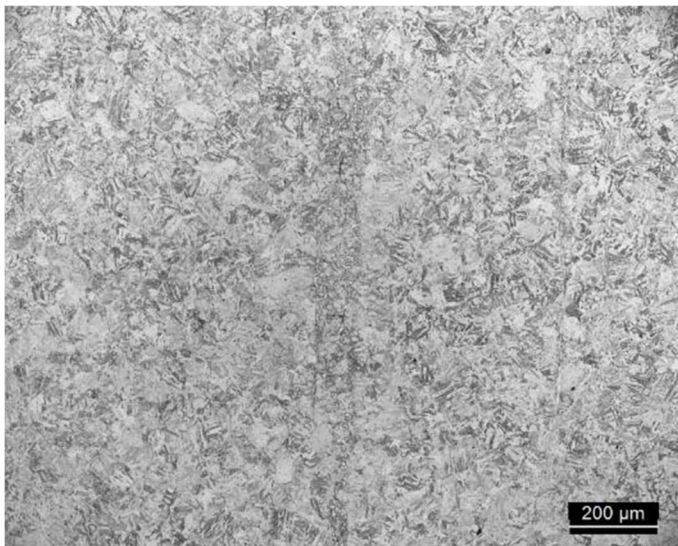
Nital Etch

Figure 17. Showing typical features of the shaft microstructure at the 0.5 radius location on the shaft, where the structure shows a more “normal” fine-grained appearance.

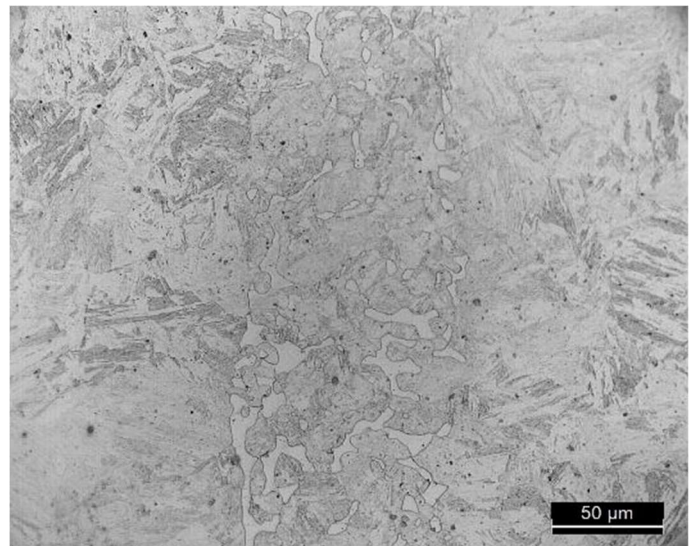


Micro-A
Nital Etch

*Center of Shaft
at fracture*

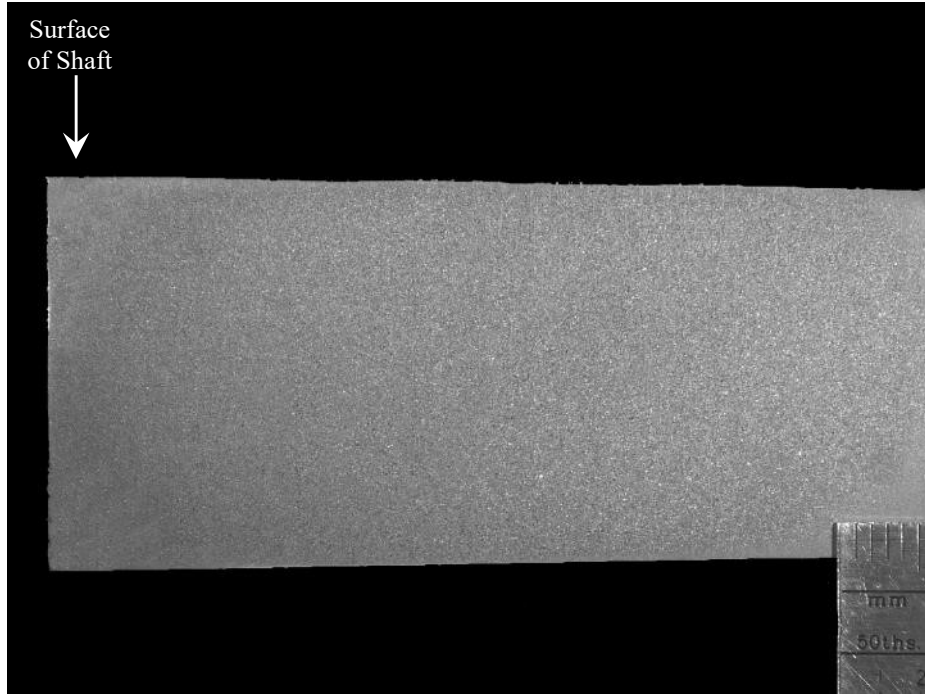


Micro-A



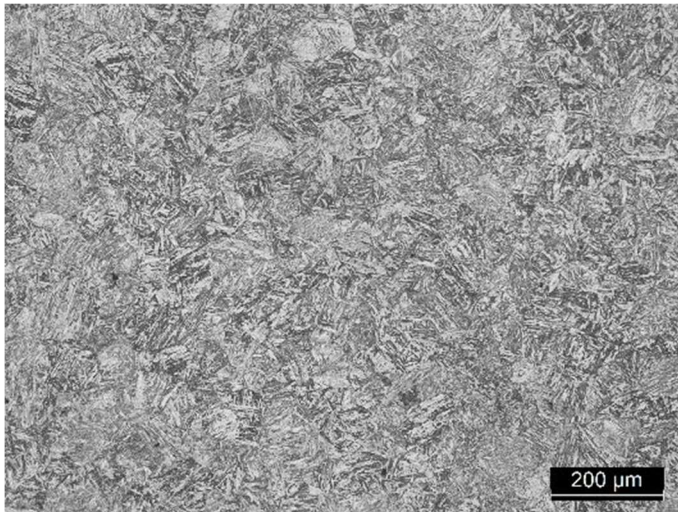
Nital Etch

Figure 18. Showing typical features of the shaft microstructure at the core (center) of the shaft, with evidence of the effects of ingotism and ferrite bands.

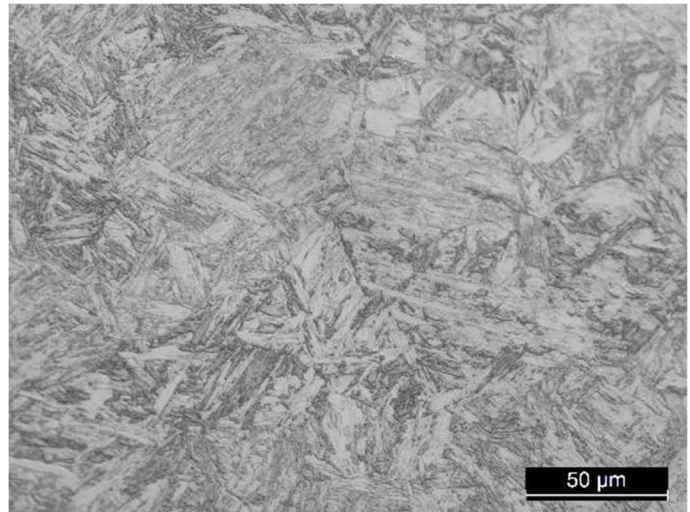


Micro-B
Nital Etch

*Surface of Shaft
at Opposite End
of Fracture*

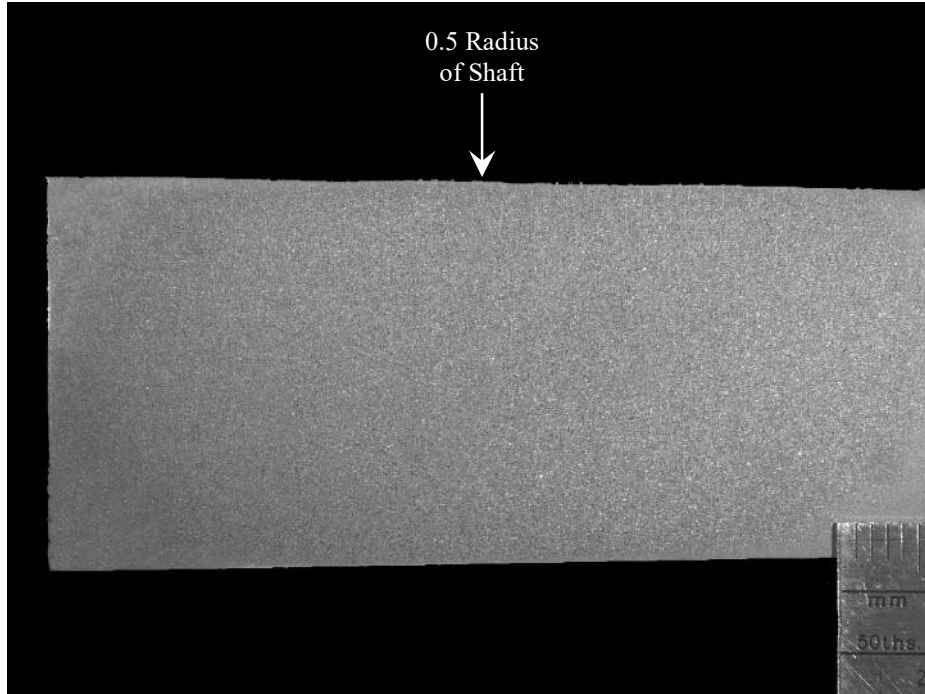


Micro-B



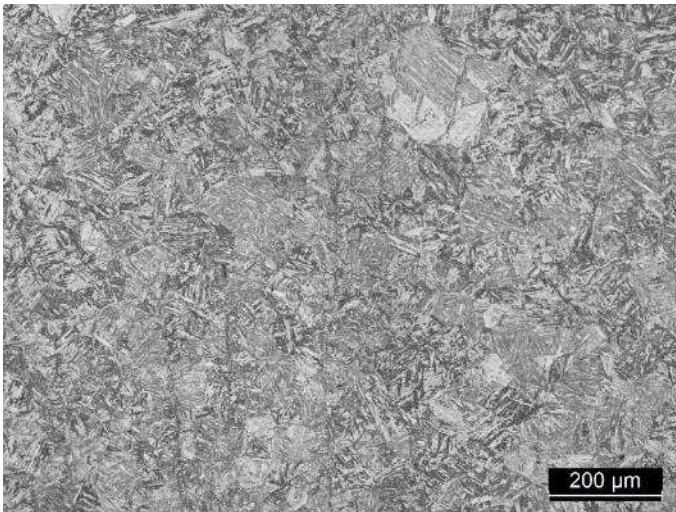
Nital Etch

Figure 19. Showing typical features of the shaft microstructure near the surface of the shaft at a location well away from the failure area; note the relatively fine-grained structure.

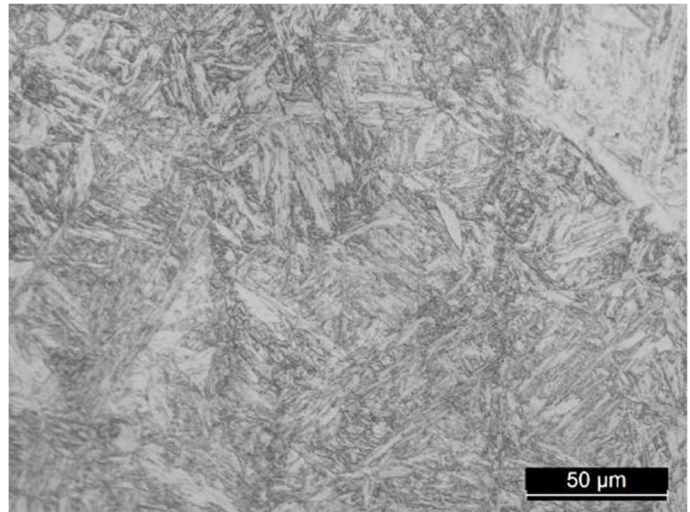


Micro-B
Nital Etch

*0.5 Radius of
Shaft at Opposite
End of Fracture*

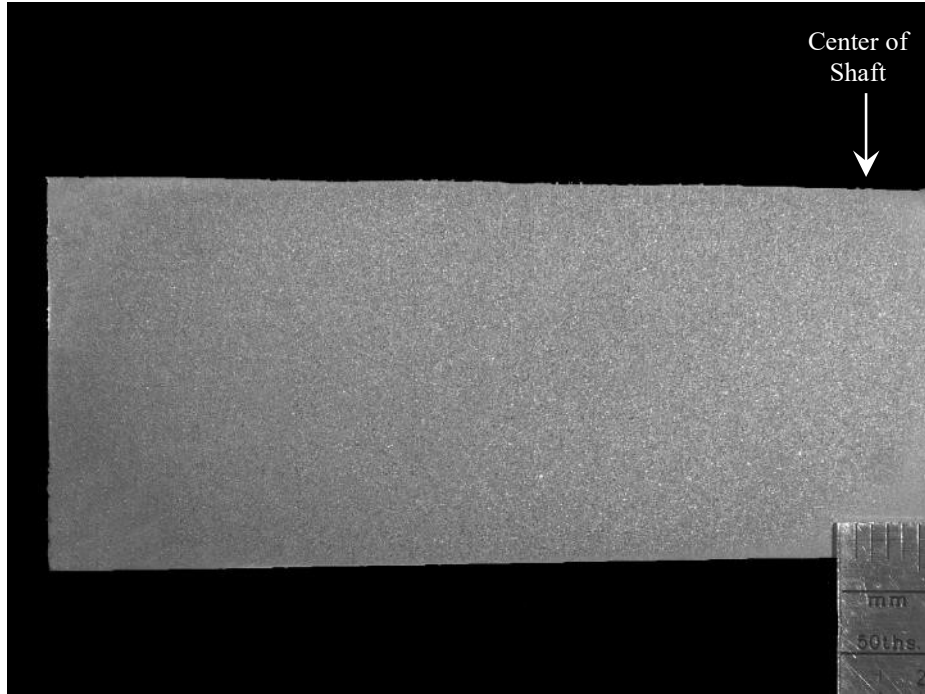


Micro-B



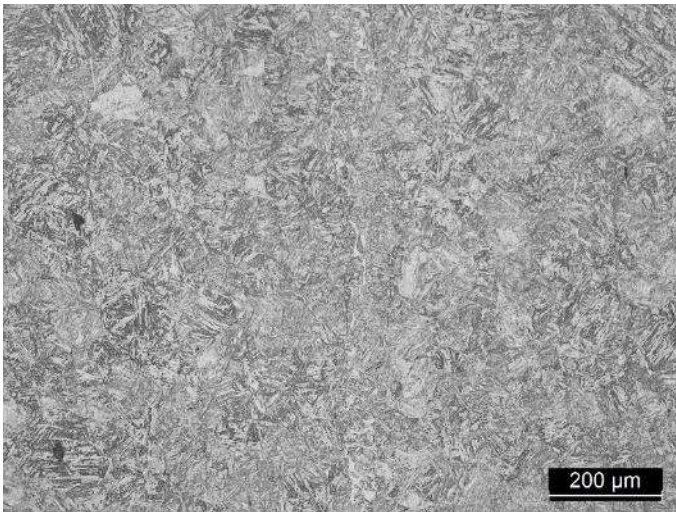
Nital Etch

Figure 20. Showing typical features of the shaft microstructure at the 0.5 radius of the shaft at a location well away from the failure area.

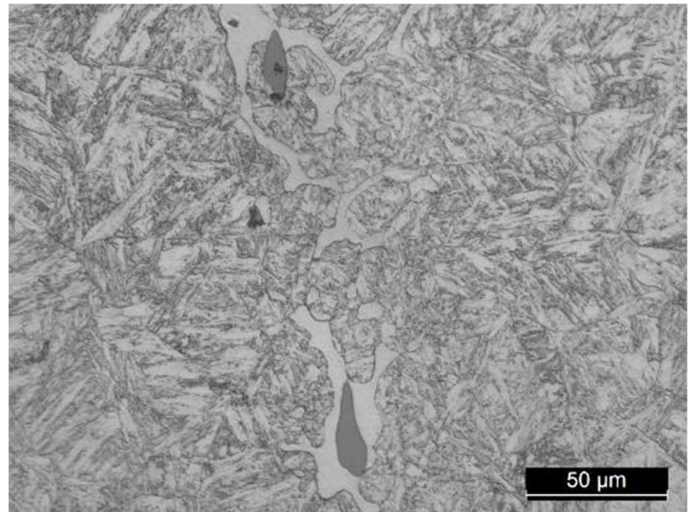


Micro-B
Nital Etch

*Center of Shaft at
Opposite End of
Fracture*



Micro-B



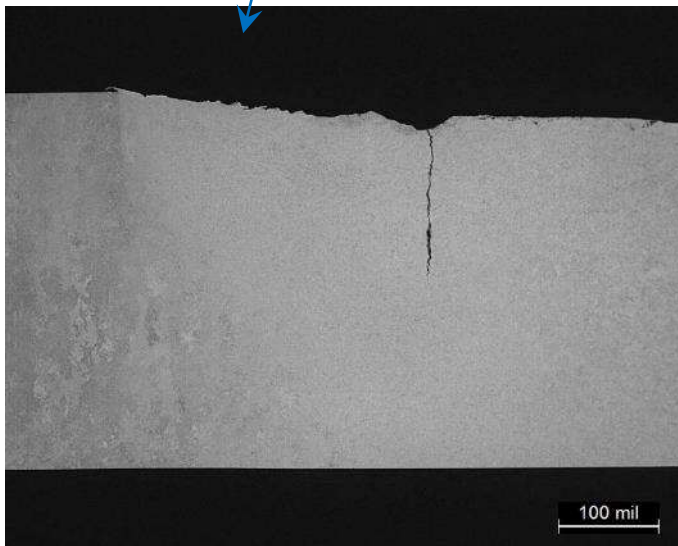
Nital Etch

Figure 21. Showing typical features of the shaft microstructure at the core (center) of the shaft at a location well away from the failure area, with evidence of the effects of ingotism and ferrite bands.

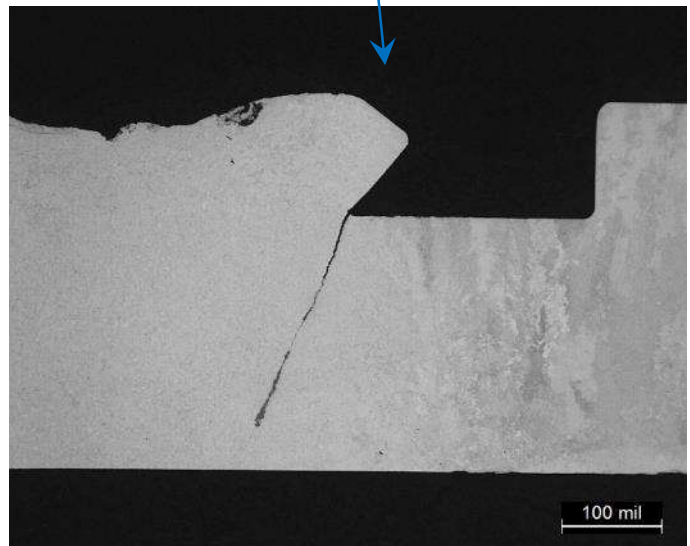


Micro-C
Nital Etch

Overheating
zones in
Sleeve

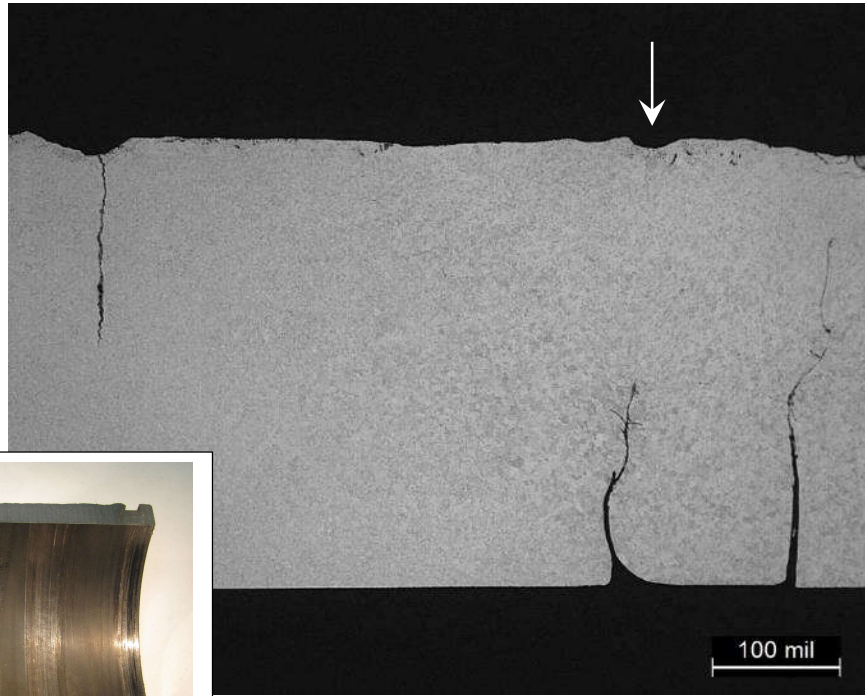


Micro-C



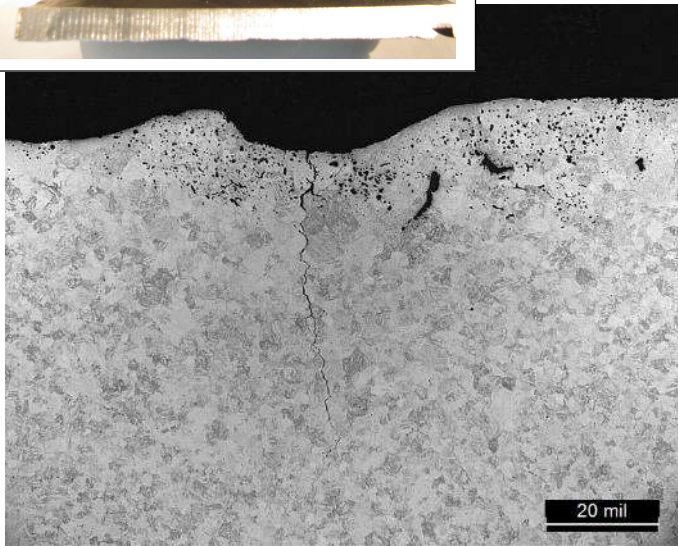
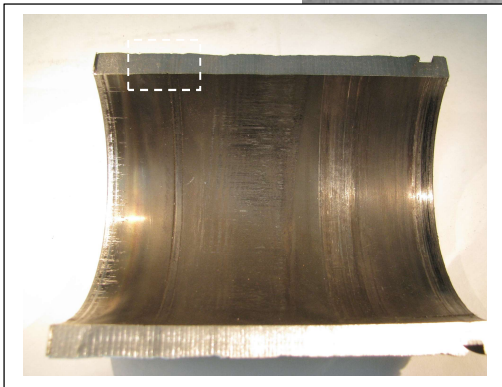
Nital Etch

Figure 22. Documenting the evidence of a pronounced heat-affected zone (HAZ) in the sleeve; this HAZ extended almost the entire length (>85%) of the sleeve. Note the cracking that had occurred in the sleeve within the overheated region.

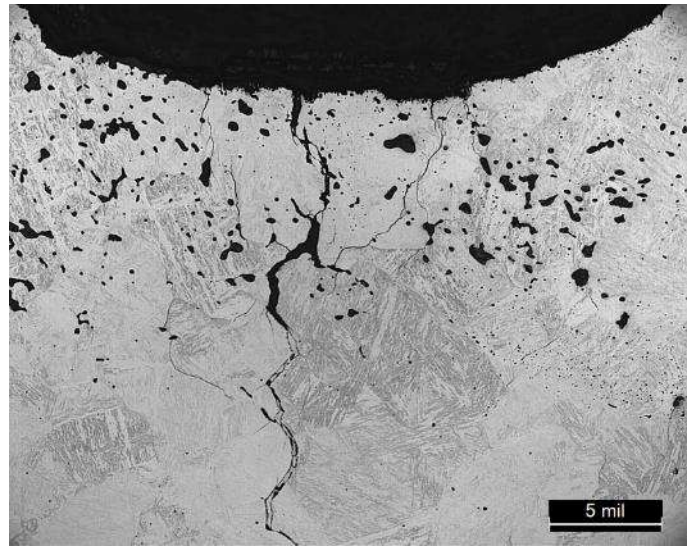


Micro-C
Nital Etch

OD Surface
Sleeve

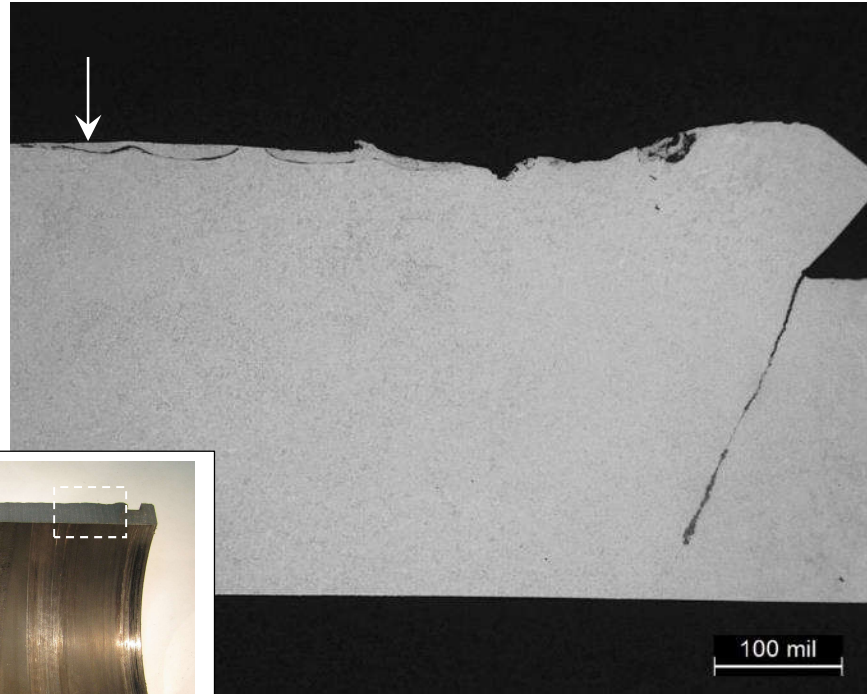


Micro-C



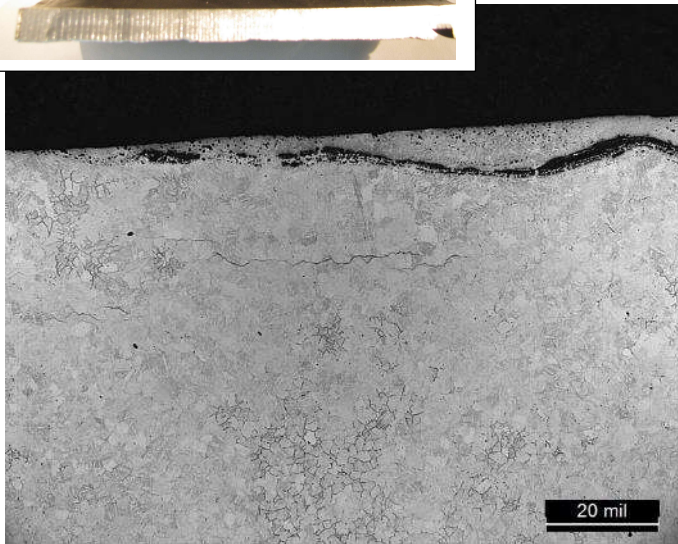
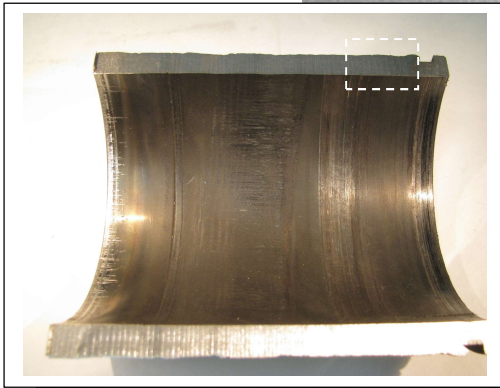
Nital Etch

Figure 23. Showing typical features of the structure of the sleeve material at the OD surface, with evidence of partial melting and re-austenitization of the structure, together with significant levels of through-thickness cracking.

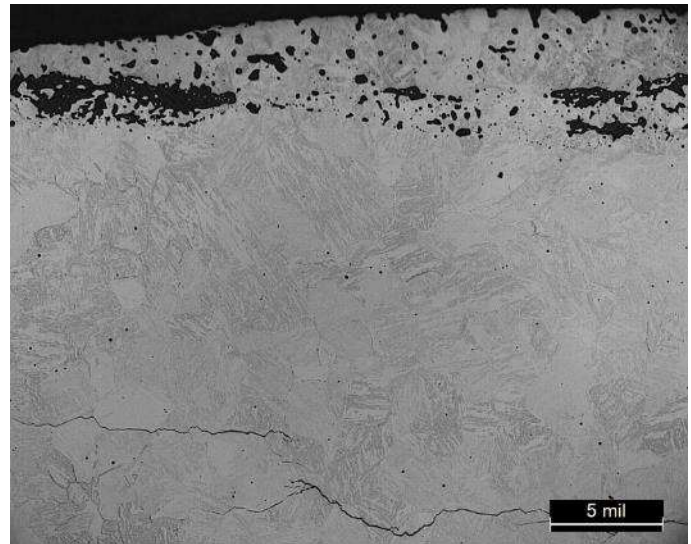


Micro-C
Nital Etch

OD Surface
Sleeve



Micro-C



Nital Etch

Figure 24. Showing typical features of the structure of sleeve at the outer surface, with evidence of partial melting and re-austenitization of the structure, as well as significant levels of axial cracking.

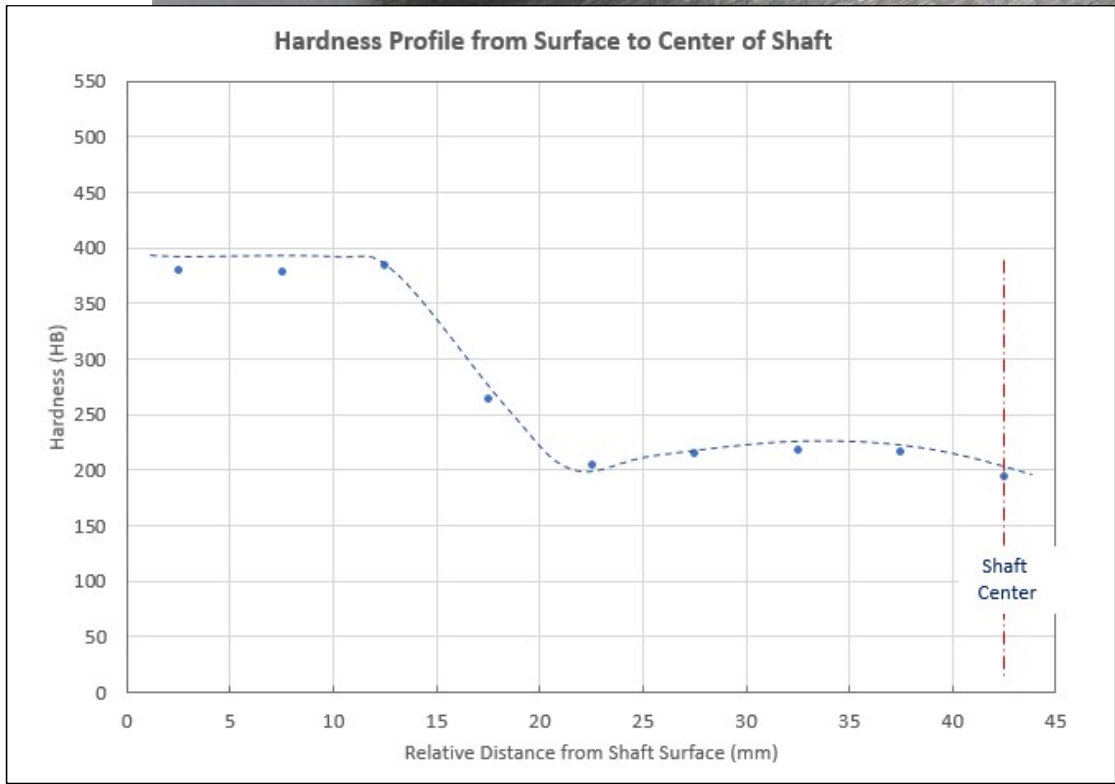
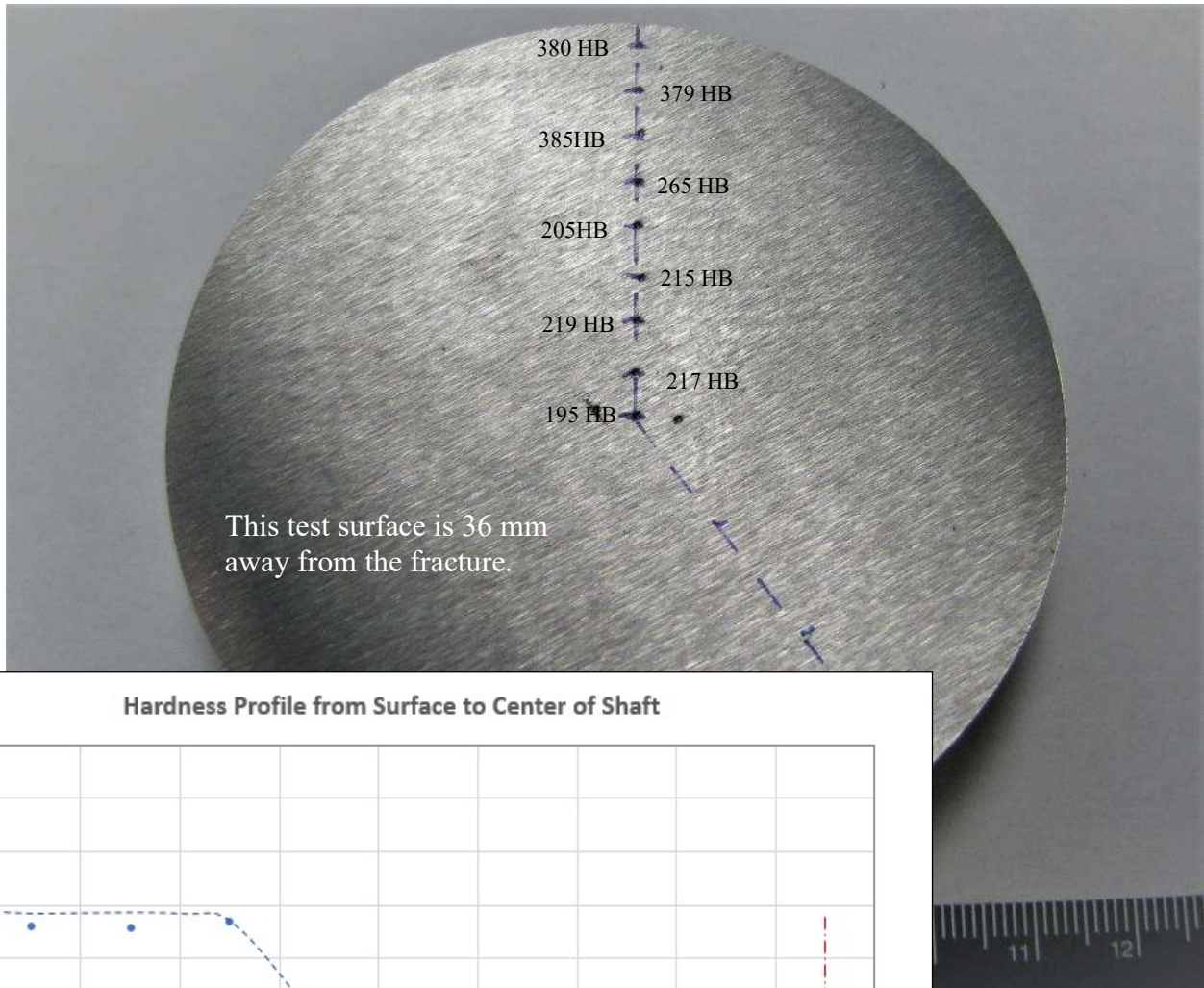


Figure 25. Showing a hardness profile produced through the thickness of the shaft (the distance from the surface to the 1st indentation is 2.5 mm and the distances between all other indentations is 5 mm). The hardness values were measured using the Rockwell C scale and these were converted to standard Brinell values.

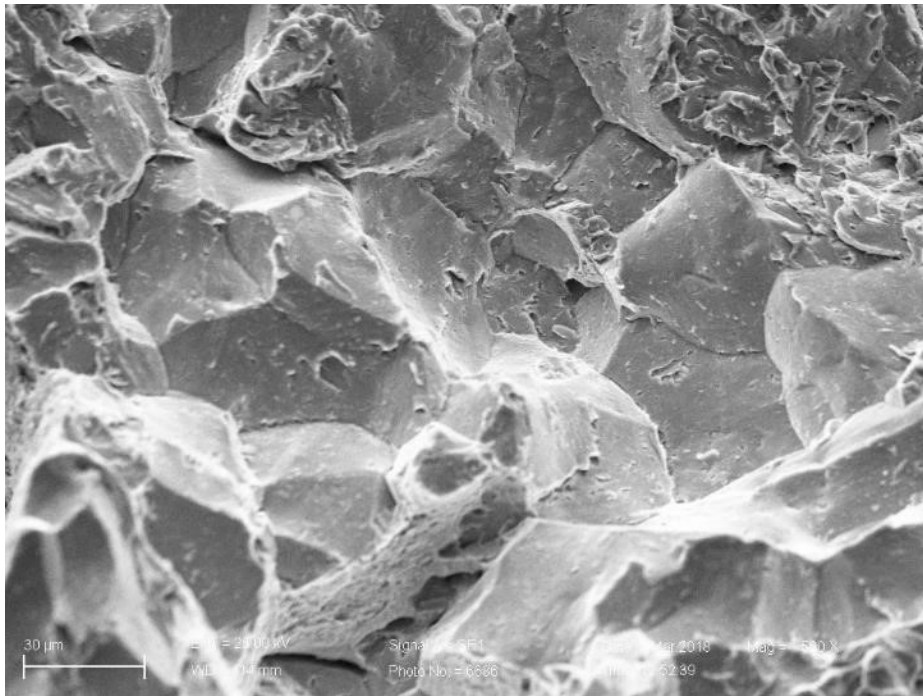
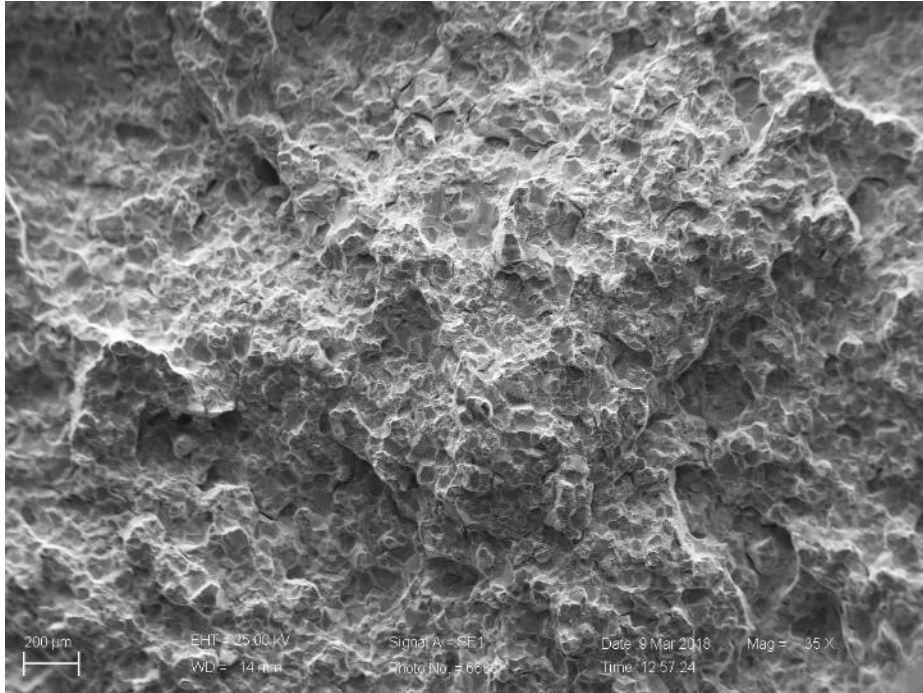


Figure 26. Shown are SEM images of typical fracture features taken from CVN specimen O1, highlighting the intergranular nature of the fracture.

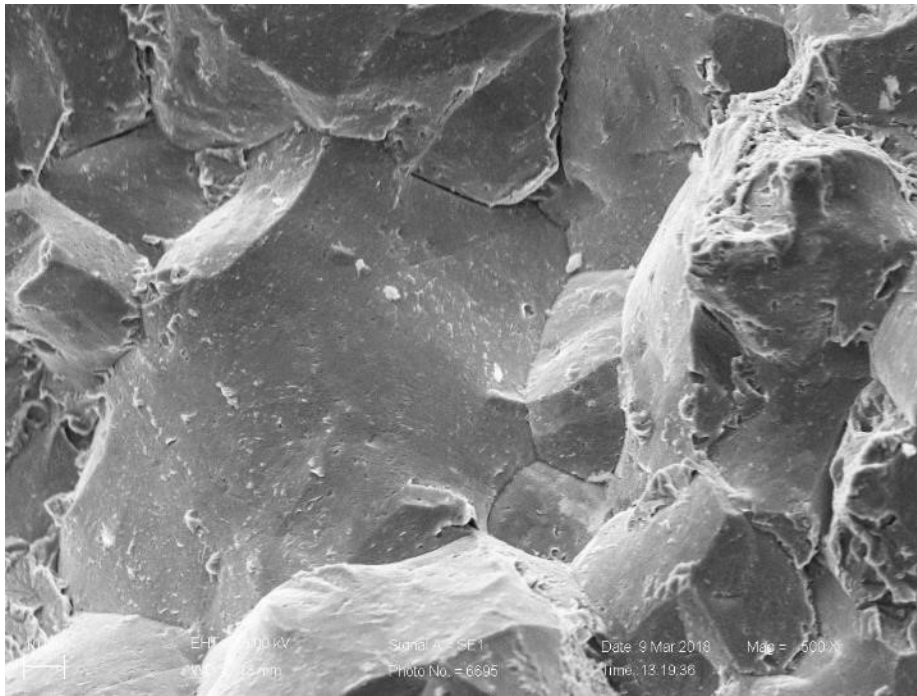
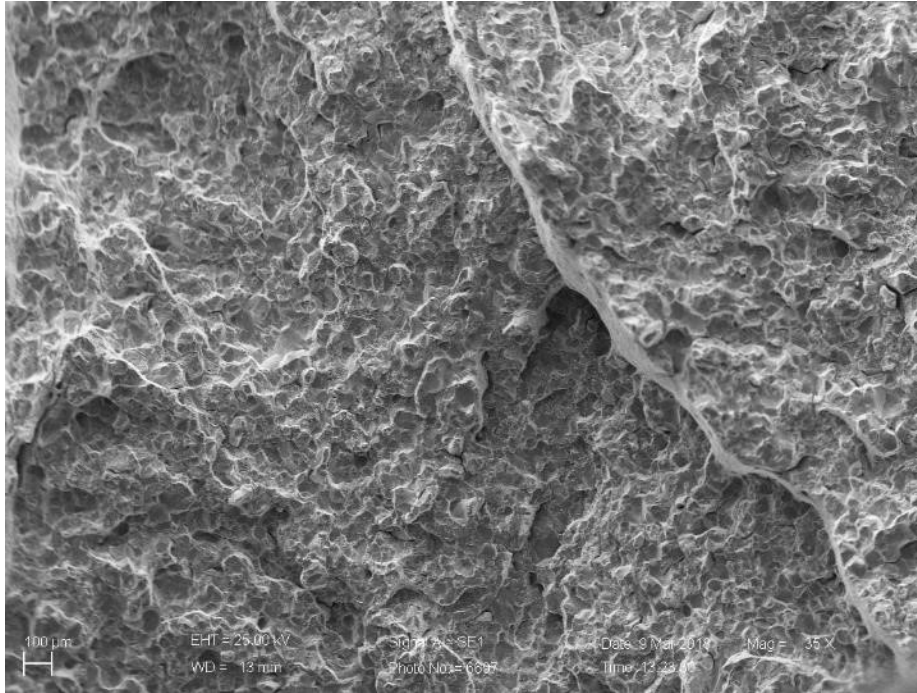


Figure 27. Shown are SEM images of typical fracture features taken from CVN specimen O3, highlighting the intergranular nature of the fracture.

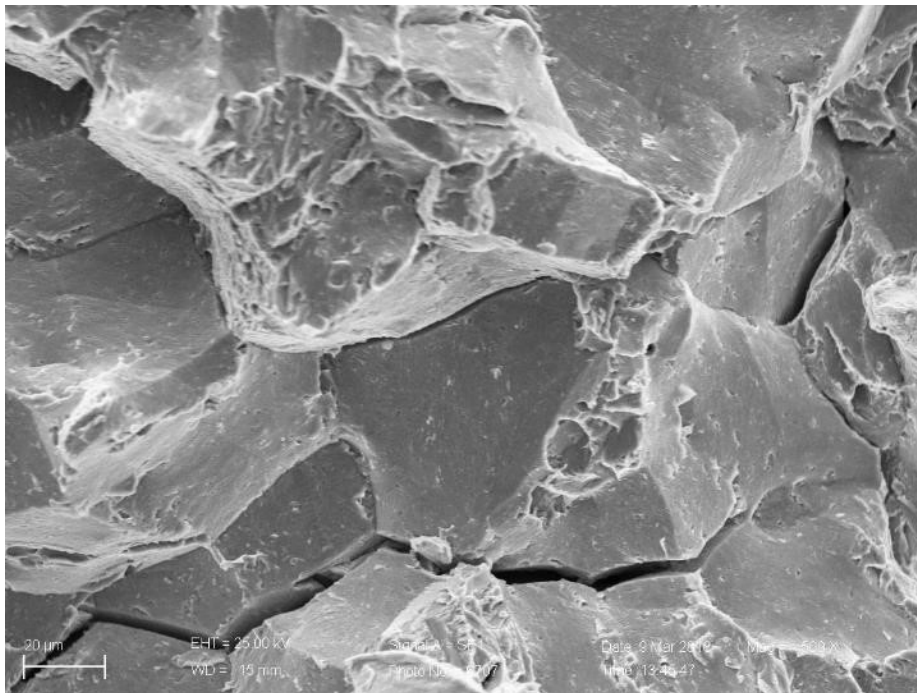
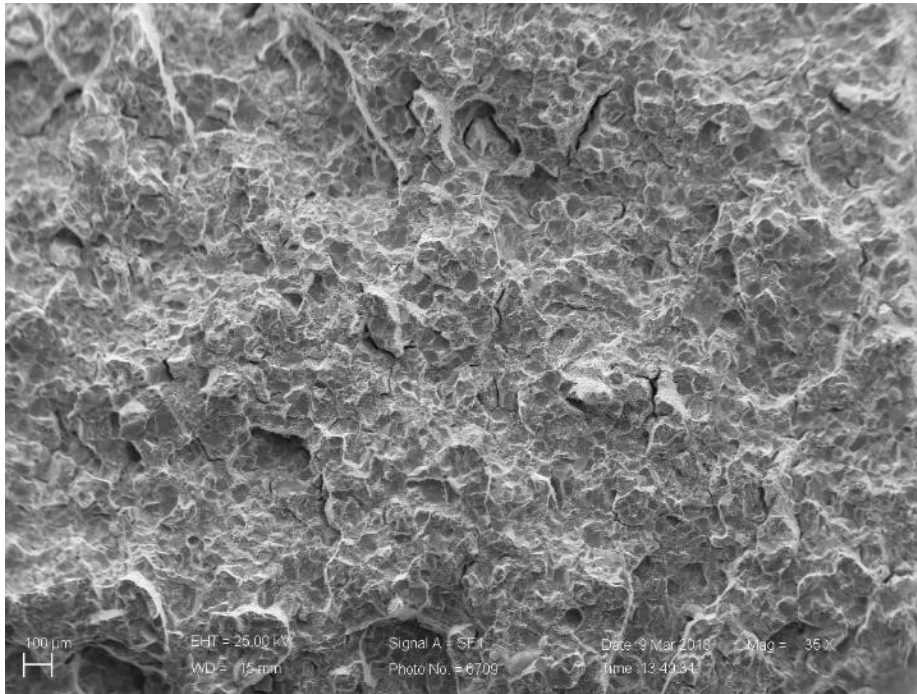


Figure 28. Shown are SEM images of typical fracture features taken from CVN specimen F1, highlighting the intergranular nature of the fracture.

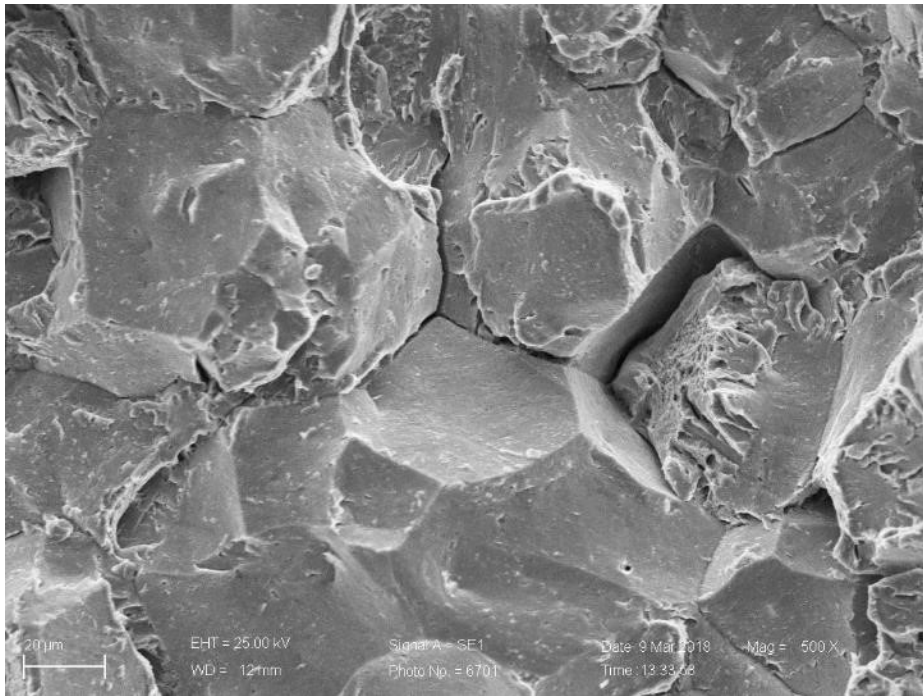
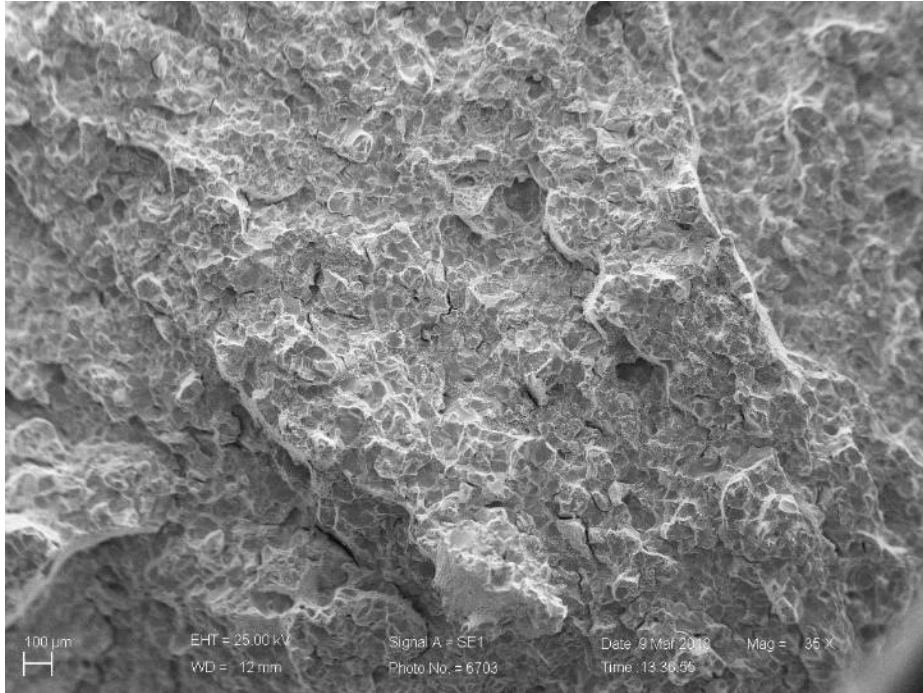


Figure 29. Shown are SEM images of typical fracture features taken from CVN specimen F3, highlighting the intergranular nature of the fracture.